The Astronomical Journal, 169:78 (19pp), 2025 February https://doi.org/10.3847/1538-3881/ad9eb3
© 2025. The Author(s). Published by the American Astronomical Society.
OPEN ACCESS

Predicting Interstellar Object Chemodynamics with Gaia

Matthew J. Hopkins[1,2], Michele T. Bannister[2], and Chris Lintott[1]
[1] Department of Physics, University of Oxford, Denys Wilkinson Building, Keble Road, Oxford, OX1 3RH, UK; matthew.hopkins@physics.ox.ac.uk
[2] School of Physical and Chemical Sciences–Te Kura Matū, University of Canterbury, Private Bag 4800, Christchurch 8140, New Zealand
Received 2024 February 7; revised 2024 November 29; accepted 2024 December 4; published 2025 January 17

Abstract

The interstellar object (ISO) population of the Milky Way is a product of its stars. However, what is in fact a complex structure in the solar neighborhood has traditionally in ISO studies been described as smoothly distributed. Using a debiased stellar population derived from the Gaia Data Release 3 stellar sample, we predict that the velocity distribution of ISOs is far more textured than a smooth Gaussian. The moving groups caused by Galactic resonances dominate the distribution. 1I/'Oumuamua and 2I/Borisov have entirely normal places within these distributions; 1I is within the noncoeval moving group that includes the Matariki (Pleiades) cluster, and 2I within the Coma Berenices moving group. We show that for the composition of planetesimals formed beyond the ice line, these velocity structures also have a chemodynamic component. This variation will be visible on the sky. We predict that this richly textured distribution will be differentiable from smooth Gaussians in samples that are within the expected discovery capacity of the Vera C. Rubin Observatory. Solar neighborhood ISOs will be of all ages and come from a dynamic mix of many different populations of stars, reflecting their origins from all around the Galactic disk.

Unified Astronomy Thesaurus concepts: Interstellar objects (52); Milky Way Galaxy (1054); Galaxy dynamics (591)

1. Introduction

The three-dimensional velocity distribution of interstellar objects (ISOs) is both complex and a valuable parameter space with which to understand the Galactic small-body population. As it is a product of their kinematics, it correlates with the chemistry of their progenitor stars, their ejection mechanisms, and the effects of Galactic dynamical processes including encounters with spiral arms and giant molecular clouds.

In the local environment—the solar neighborhood, and specifically the region which our observable volume of the solar system samples—the velocity distribution affects a range of factors. Locally, it can affect ISO detectability within the solar system volume (P. J. Francis 2005). As a consequence, it affects estimates of the total Galactic population size, therefore affecting inference on the various ISO production mechanisms (A. Moro-Martìn et al. 2009). The breadth of ISO velocities also limits the potential for encounter and sampling visits to ISOs by spacecraft, which have finite Δv (K. Moore et al. 2021; G. H. Jones et al. 2024). Finally, it also affects what can be inferred of the origin history of the two currently detected ISOs, 1I/'Oumuamua and 2I/Borisov.

Previous works considering a velocity distribution for ISOs consistently assume that it is equal to the stellar distribution, and assume that the stellar distribution is a multivariate Gaussian (F. L. Whipple 1975; Z. Sekanina 1976; T. A. McGlynn & R. D. Chapman 1989; S. A. Stern 1990; N. V. Cook et al. 2016; T. Engelhardt et al. 2017; D. Seligman & G. Laughlin 2018; J. C. Forbes & A. Loeb 2019; D. Marčeta & B. Novaković 2020; D. J. Hoover et al. 2022; D. Marčeta 2023; D. Marčeta & D. Z. Seligman 2023). However, J. Binney & M. Merrifield (1998) caution that the local stellar velocity distribution is not well described by a Gaussian; in particular, being smooth, these distributions will miss any structure and features of the velocity distribution of objects in the solar neighborhood.

The stellar velocity distribution is not smooth: It has strong overdensities called moving groups and branches, known since A. S. Eddington (1906) and well-studied since Hipparcos (W. Dehnen 1998; J. Skuljan et al. 1999). These are not coeval (B. Nordström et al. 2004; T. Bensby et al. 2007; T. Antoja et al. 2008; B. Famaey et al. 2008), so while originally thought to be dispersed star clusters, they are now understood to be temporary structures, sculpted by resonances with the Galaxy's spiral arms and bar—which themselves may be transient (A. C. Quillen et al. 2011; T. Antoja et al. 2018; J. A. S. Hunt et al. 2018, 2019; T. A. Michtchenko et al. 2018; P. Ramos et al. 2018; W. H. Trick et al. 2021; S. Lucchini et al. 2023). In the age of Gaia, the local stellar velocity distribution is now known with exquisite precision. Additionally, protoplanetary disk modeling is now able to link stellar chemical abundances to aspects of planetesimal composition; for example, N. C. Santos et al. (2015), who predict the iron mass fraction of exoplanets, and B. Bitsch & C. Battistini (2020), who predict planetesimal composition both inside and outside the water-ice line. Thus variations in the physical composition of ISOs, such as their water mass fraction, can be mapped to their home system's stellar metallicity—making it possible to use ISOs as sensitive tracers of the Galactic star formation history (C. Lintott et al. 2022). This strongly suggests that combining predictions of ISO physical compositions with their three-dimensional velocity distributions will reveal structure. For consistency with Galactic evolution terminology, we refer to this as their "chemodynamics" (as used in, e.g., A. Burkert & G. Hensler 1987; J. Binney & E. Vasiliev 2024).

We use current knowledge of the local stellar population within 200 pc of the Sun to model the local ISO distribution. Using the inference framework developed in M. J. Hopkins

Original content from this work may be used under the terms of the Creative Commons Attribution 4.0 licence. Any further distribution of this work must maintain attribution to the author(s) and the title of the work, journal citation and DOI.

et al. (2023) and Gaia Data Release 3 (DR3) measurements, we explore the kinematics, specifically the velocity distributions, and the chemodynamics of the local population structure of ISOs. We term this model the Ōtautahi-Oxford model. This is the first such study to account for metallicity effects and stellar death, or examine the three-dimensional kinematic structures, though T. M. Eubanks et al. (2021) estimate the ISO speed distribution from Gaia early Data Release 3 by applying a volume sampling rate to a subset of the Gaia Catalog of Nearby Stars (Gaia Collaboration et al. 2021) with radial velocities.

We show that the local velocity distribution of ISOs is richly featured and the velocity of an ISO correlates with the metallicity and age of its origin star, and therefore its own composition and age. We demonstrate the sample sizes needed to distinguish between our predicted ISO velocity distribution and smooth Gaussian distributions. This chemodynamic texture will be perceptible by upcoming solar system surveys, such as the Vera C. Rubin Observatory Legacy Survey of Space and Time (LSST; Ž. Ivezić et al. 2019).

2. Method

In M. J. Hopkins et al. (2023), we used positions and elemental abundances of stars from APOGEE (H. Jönsson et al. 2020) for modeling the ISO spatial distribution over a large swath of the Galactic disk; here our focus is the velocity distribution in the solar neighborhood, so we use Gaia (Gaia Collaboration et al. 2016). We first use Gaia measurements of stellar proper motion, radial velocity, metallicity, and age to calculate the distribution in these properties of the stellar population within 200 pc of the Sun. We account for the survey's selection effects on each of these measurements. First, we use the methods of T. Cantat-Gaudin et al. (2023) and A. Castro-Ginard et al. (2023) to calculate a selection function in color and magnitude; we then calculate our own effective selection function (ESF) in age, metallicity, and distance, simultaneously accounting for stellar death (Section 2.1). As in M. J. Hopkins et al. (2023), this lets us recover the distribution of the sine morte stellar population: what the stellar population would be if stars did not die (Section 2.2).[3] From our debiased stellar distribution, we then predict the ISO distribution: We combine this stellar population with the protoplanetary disk chemical model of B. Bitsch & C. Battistini (2020), and the assumptions in Section 2.3 on the ejection of planetesimals and their motion in the Galaxy. This gives us a predicted distribution of ISOs in the solar neighborhood in velocity, age, and composition. Finally, to predict the distribution of ISOs entering the inner solar system, where they will be detectable by sky surveys such as the Vera C. Rubin Observatory's LSST, we apply a gravitationally focused volume sampling rate to account for the motion of ISOs relative to the Sun (Section 2.4).

2.1. Gaia and Its Selection Function

Gaia DR3 provides a comprehensive data set of the stars in our part of the Galaxy (Gaia Collaboration et al. 2023). We first obtain a subset of Gaia DR3, requiring the presence of high-precision measurements of velocity, metallicity, and age in our sample. We define the solar neighborhood as a sphere around the Sun out to the somewhat arbitrary distance of 200 pc, similar in scale to the distances used by T. Antoja et al. (2018) and A. Recio-Blanco et al. (2023), so we take stars with Gaia trigonometric parallax $\geqslant$5 mas.[4] To ensure these parallaxes are accurate, we require `parallax_over_error` > 10, and in order to calculate the three-dimensional velocities of each star, we require a radial velocity to have been measured and have an error of less than 5 km s^{-1}. We require the availability of General Stellar Parametrizer from Spectroscopy (GSP-Spec) metallicity [M/H] and GSP-Spec-based Final Luminosity Age Mass Estimator (FLAME) ages, both of which are measured using data from the Radial Velocity Spectrometer (RVS; M. Cropper et al. 2018): [M/H] is measured by fitting RVS spectra to synthetic spectra from a five-parameter stellar atmosphere model (A. Recio-Blanco et al. 2023), and GSP-Spec-based FLAME age is calculated from these atmospheric parameters and isochrone fitting (M. Fouesneau et al. 2023). Comparing to literature values, GSP-Spec [M/H] estimates show no bias and a dispersion of 0.13 dex (A. Recio-Blanco et al. 2023), while FLAME ages have mean biases and dispersions of only 0.1–0.3 Gyr and 0.25 Gyr, respectively (M. Fouesneau et al. 2023). To ensure accurate ages, we remove giants from the sample by requiring `flags_flame_spec` $= 0$ (O. L. Creevey & Y. Lebreton 2022; O. L. Creevey et al. 2023; M. Fouesneau et al. 2023). These measurements have the highest accuracy available; while only present for bright stars ($G \lesssim 14$), within 200 pc we can account for the selection effects these cuts induce. This yields a sample of 201,863 observed living stars. Though Gaia does detect white dwarfs (e.g., N. P. Gentile Fusillo et al. 2021; F. M. Jiménez-Esteban et al. 2023), it does not measure their age or composition, so for consistency we do not include them here.

Gaia, like any survey, has selection effects: It does not observe all stars, does not make every measurement for each of the stars it observes, and does not choose stars to make measurements for in an unbiased way. Thus in order to reconstruct the true underlying stellar population from our subsample, our subsample needs to be debiased.

First, we estimate the subsample selection function (SSF): the fraction of stars in the underlying stellar population that make it into the subsample we define above, as a function of color, magnitude, and on-sky position. This is equal to the fraction of the stars at each color, magnitude, and on-sky position in the Gaia catalog that is also in our subsample, multiplied by the catalog completeness. The catalog completeness is the fraction of the underlying population that makes it into the Gaia catalog (i.e., has at least one measurement recorded), however T. Cantat-Gaudin et al. (2023) find that for magnitudes brighter than the limit of our subsample ($G \lesssim 14$) the catalog is 100% complete, so we do not need to calculate this. This means we can estimate SSF following the method of A. Castro-Ginard et al. (2023). A. Castro-Ginard et al. (2023) find that the selection function for the subsample of stars with a radial velocity measurement depends on G magnitude, $G - G_{\rm RP}$ color, and on-sky position. Since the additional measurements we require (GSP-Spec [M/H] and GSP-Spec-based FLAME age) are both computed from the output of the RVS, we follow A. Castro-Ginard et al. (2023) in assuming that our SSF depends on magnitude, color, and on-sky position. The method of A. Castro-Ginard et al. (2023) calls for counting the number of stars in the subsample k and number of stars in

[3] We continue use of this from M. J. Hopkins et al. (2023): sine morte, Latin for "without death," ['si:ne 'mɔrte] IPA pronunciation, or "seen-ay mort-ay."

[4] Note, due to a parallax bias of size ~10 μas (L. Lindegren et al. 2021) this will not correspond to exactly 200 pc.

catalog n in bins in magnitude, color, and on-sky position (using Hierarchical Equal Area isoLatitude Pixelation, or HEALPix; K. M. Górski et al. 2005). The SSF is then estimated in each bin as $(k+1)/(n+2)$ with an uncertainty of $\sqrt{\frac{(k+1)(n-k+1)}{(n+2)^2(n+3)}}$. We define our subsample as having measurements of radial velocity, [M/H], and age with the same cuts on errors and flags as our data described above; the exact query to the Gaia archive used is listed in Appendix A. We calculate the SSF in bins in color and magnitude of width $\Delta G = 1$ and $\Delta(G - G_{\rm RP}) = 0.2$. Following A. Castro-Ginard et al. (2023), we group the Galactic polar caps (Galactic latitudes $|b| > 30$ deg) and bin the rest of the sky in HEALPix level 2, a level that retains the smooth shifts in the selection function. These bins have a larger width in magnitude and on-sky position than the binning of A. Castro-Ginard et al. (2023); as our subsample is smaller, requiring more measured quantities, we use broader bins to retain statistical quality. To ensure uniformity across the sky and a low fractional uncertainty in the ESF described below, we set the SSF equal to zero in all color–magnitude bins with any on-sky bin where $k < 2$. This does not affect any color–magnitude bins where a significant number of stars are observed, retaining 98% of the stars in the subsample. This gives us the selection function in magnitude, color, and sky position.

Second, we estimate the ESF: the fraction of stars in the underlying stellar population that makes it into the subsample we define above, as a function of their metallicity, age, distance, and on-sky position. We estimate this by combining the SSF, a function of color and magnitude, with PARSEC isochrones (A. Bressan et al. 2012; P. Marigo et al. 2017), stellar models which predict the color and magnitude stars with a given metallicity, age, and distance have at each mass. We estimate the ESF by integrating over mass the SSF weighted by a Kroupa initial mass function (IMF; P. Kroupa 2001) along PARSEC isochrones, calculating the fraction of the modeled stellar population that would make it into our subsample at each metallicity, age, distance, and on-sky position.

The reason we need to use the ESF to debias our sample is that the SSF is nonzero only in a narrow color range ($0.2 \leqslant G - G_{\rm RP} < 0.6$), so we cannot account for the contributions of stars outside of this range directly. Conversely, the ESF remains nonzero across almost all of parameter space, meaning the entire stellar population within 200 pc can be reconstructed.

We calculate the ESF using PARSEC isochrones at [M/H] between −1.45 and 0.65 spaced by 0.1 and ages from 0.5 Gyr to 13.5 Gyr spaced by 1 Gyr, and the universal IMF of P. Kroupa (2001). When converting between absolute and apparent magnitudes we do not account for dust extinction, as within 200 pc from the Sun this is limited to 1 mag at most in the G band (G. M. Green et al. 2019; R. Lallement et al. 2022).

Stars can be assumed to form with a consistent IMF (G. Chabrier 2001; P. Kroupa et al. 2013), but to quantify how varying the IMF used affects our results, we also calculate an alternative ESF using the log-normal IMF of G. Chabrier (2003). Since our results consist of relative distributions and not absolute values, to compare the two ESFs we scale them to have the same mean value, then calculate the mean fractional difference between the two to be only 0.8%. Thus the choice of IMF does not affect our results, and we use the Kroupa-based ESF for the rest of this work.

The final effect we account for is stellar death. Stars born throughout Galactic history emit ISOs, and we expect ISOs to outlive their parent stars: For instance, $\gtrsim$10 km-diameter Oort cloud comets have survived 4.5 Gyr in an interstellar environment with little erosion (A. Guilbert-Lepoutre et al. 2015), so similar-scale ISOs will largely remain intact. This means we cannot use the distribution Gaia observes of only the currently living stars, or the proportion of young ISOs would be overestimated: Figure 1 (Age) shows the difference between the age distributions of the raw Gaia data points and the reconstructed sine morte distribution. Instead, we must estimate what the stellar population would be without stellar death: the sine morte stellar population. We account for this in our model at the same time that we account for Gaia's selection effects: We define the ESF as the fraction of all stars ever formed (i.e., the fraction of the sine morte population) at a given age, metallicity, on-sky position, and distance that would be observed.

Unlike the SSF, the ESF is nonzero for almost all of its parameter space, meaning all populations are represented by at least a fraction of their stars in the Gaia sample and thus their contributions can be accounted for. The only exceptions to this are in bins at distances closer than 25 pc, so to ensure uniformity we cut the few stars with observed parallax >40 mas, leaving a final data sample of size 201,426.

We list the ADQL queries made to the Gaia archive to retrieve all data sets in Appendix A.

2.2. The Local Sine Morte Stellar Distribution

In the previous section, we described how we acquired a sample of stars from Gaia with a set of observed properties, and defined the ESF: the fraction of the underlying sine morte stellar population included in our sample as a function of their observed properties. This allows us to debias our observed sample and estimate the underlying distribution of these properties in the sine morte stellar population. We do this by treating our sample of stars as a weighted sampling of the sine morte population, weighted by the inverse of the value of the ESF for each star. Since the ESF is the fraction of sine morte stars included in our sample, its inverse gives the number of stars in the underlying sine morte population represented by each observed star. The median value of the ESF over the stars in our sample is 1/22.5, meaning this median observed star represents 22.5 stars in the sine morte population. This gives us the solar neighborhood sine morte stellar distribution in velocity, age, and metallicity [M/H], plotted in Figure 1.

In Figure 1 (In-Plane Velocity and Out-of-Plane Velocity) the velocity distribution is plotted in its right-handed Cartesian components relative to the Sun's velocity: U toward the Galactic center, V in the direction of Galactic rotation, and W out of the plane of the Galaxy. Immediately obvious is the rich structure in the stellar velocity distribution: the moving groups and branches (compare to Figure 5 of T. Antoja et al. 2008, for identification). As described in the Introduction (Section 1), these overdensities are caused by resonances with the Galactic spiral arms and bar carving out furrows in the velocity distribution, and are not dispersed clusters. There is less structure in the W distribution than the U and V distributions. With a yellow square we mark the local standard of rest (LSR; R. Schönrich et al. 2010), the velocity that a star on a circular orbit would have in an azimuthally smoothed Galactic potential, which approximates the actual potential.

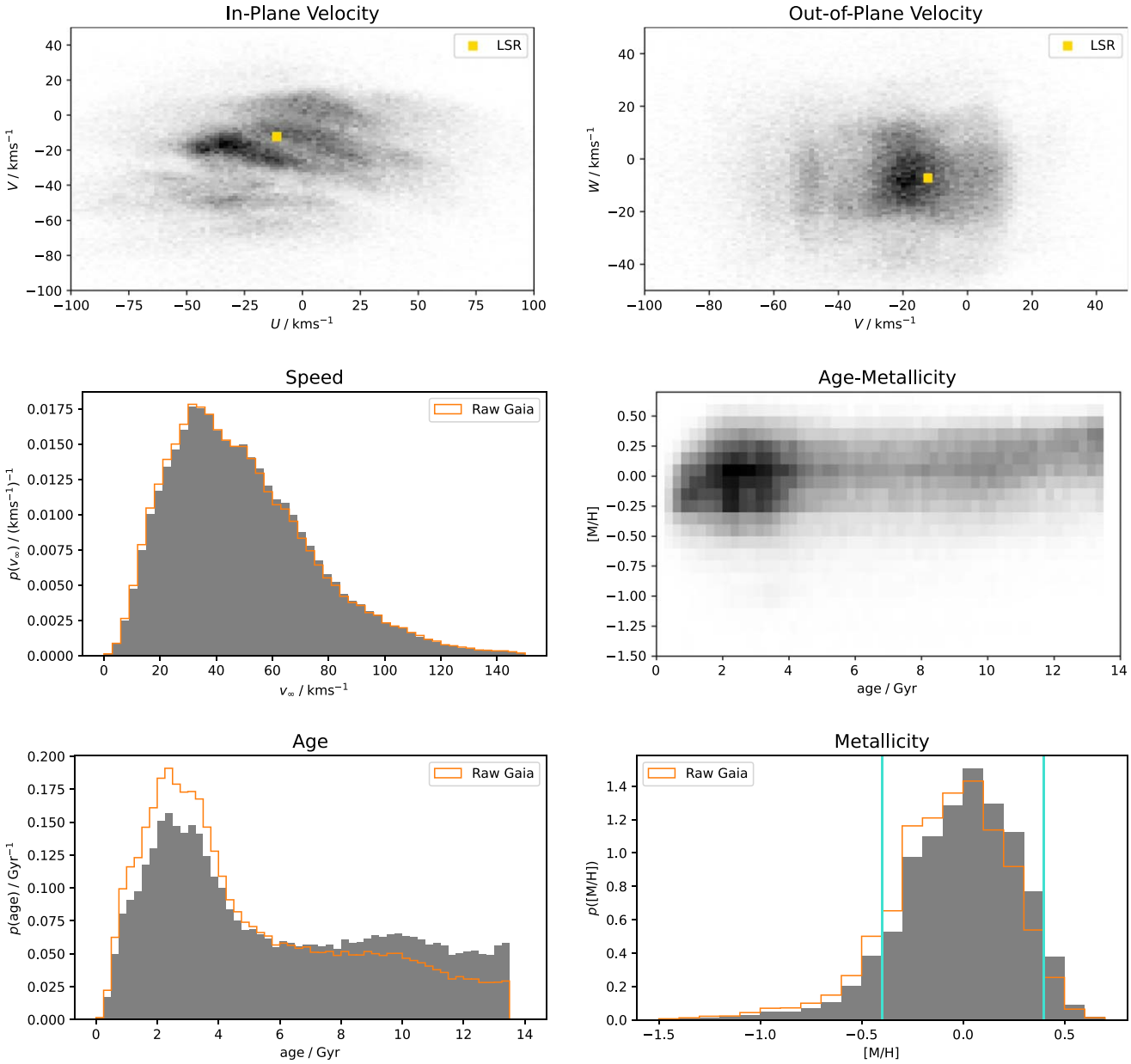

Figure 1. Distributions of the sine morte stellar population in velocity, age, and [M/H]. U is the component of velocity toward the Galactic center, V in the direction of motion around the Galactic center, and W out of the plane of the Galaxy, each relative to the Sun's velocity. Both one-dimensional and two-dimensional histograms are normalized to integrate to unity. In orange unfilled histograms we have also plotted the distribution of the raw Gaia sample, without accounting for selection effects or stellar death, for comparison. The vertical lines on the [M/H] distribution are the limits of the protoplanetary disk chemical model.

We measure an age distribution for the solar neighborhood plotted in Figure 1 (Age) that is similar to that of B. Nordström et al. (2004). We also recover a known feature of the stellar population of the solar neighborhood: a flat age–metallicity relation, with a large scatter in metallicity at all ages, meaning stars of all metallicities are found at all ages (Figure 1, Age–Metallicity). The feature is surprising, as one would expect stellar nucleosynthesis to cause the metallicity of stars to increase over time and thus decrease with age, however it is attested in many surveys of stars (B. Edvardsson et al. 1993; M. Haywood et al. 2013) as well as surveys of white dwarfs (A. Rebassa-Mansergas et al. 2021). The reason for the solar neighborhood's flat age–metallicity relation is debated, with explanations including an inside-out formation of the Galactic disk with radial migration (J. A. Sellwood & J. J. Binney 2002; R. Schönrich & J. Binney 2009), and a two-phase formation of the Galactic disk (M. Haywood et al. 2013).

2.3. Stars Produce Interstellar Objects

To predict the solar neighborhood ISO distribution from the sine morte stellar distribution, we follow a similar method to M. J. Hopkins et al. (2023). As in M. J. Hopkins et al. (2023, their Section 3.1), we map stellar metallicities to ISO compositions. The model of B. Bitsch & C. Battistini (2020) generates a clear trend for a planetesimal's water mass fraction f_{H_2O} with stellar metallicity, for planetesimals beyond the water-ice line (see their Figure 10). We expect the majority of ISOs to originate in this region due to the greater number of planetesimals and the higher

efficiencies of ejection mechanisms at larger distances from the central star (A. Fitzsimmons et al. 2023). Though the relation in B. Bitsch & C. Battistini (2020) correlates f_{H_2O} with [Fe/H], the relative abundance of iron specifically, this is well approximated by Gaia's overall metallicity [M/H] for the thin-disk, non-alpha-enhanced majority of stars in the solar neighborhood (M. Salaris & S. Cassisi 2005). We therefore use this water mass fraction as our defining compositional property for the chemodynamic analysis. B. Bitsch & C. Battistini (2020) predict that the water mass fraction of planetesimals decreases with increasing metallicity. This chemical model is limited to metallicities within $-0.4 \leqslant [M/H] \leqslant 0.4$, corresponding to $0.07 \leqslant f_{H_2O} \leqslant 0.51$; the majority of our ISOs do lie within these limits. Outside of this range, we assume that the relationship between f_{H_2O} and [M/H] continues to be monotonic, with f_{H_2O} remaining high beyond the low-[M/H] limit and remaining low beyond the high-[M/H] limit.

Though we assume here that the majority of ISOs form beyond the water-ice line, there have been several mechanisms suggested which may eject planetesimals from much closer to their parent star (e.g., M. Ćuk 2018; R. R. Rafikov 2018; A. C. Childs & R. G. Martin 2022). These ISOs would be chemically distinct as they would most likely be devolatilized. Future modeling should consider the likely contribution of these populations to the observed ISO fraction, but will need detailed consideration of nonlinear processes within the disk as well as a more sophisticated chemical treatment. However, we note that both discovered ISOs so far appear to originate from beyond the H_2O ice line, with the nongravitational (NG) acceleration of 1I suggesting the presence of volatiles (M. Micheli et al. 2018) and 2I originating from beyond the CO ice line (D. Z. Seligman et al. 2022). Additionally, even for planetesimals formed beyond the water-ice line, the one-to-one relation between f_{H_2O} and [M/H] in B. Bitsch & C. Battistini (2020) is a simplification, as in reality stars of one metallicity will produce ISOs with a range of compositions. N. Cabral et al. (2023) show that though the exact mass fraction values in the relation are uncertain, they confirm the trend of decreasing f_{H_2O} with [Fe/H] to be robust.

Since the mass of planetesimal-forming metals in a protoplanetary disk appears proportional to the metal fraction of its central star (e.g., C. X. Lu et al. 2020), we assume that the number of ISOs produced by a star of a given metallicity [M/H] is proportional to $10^{[M/H]}$. We explored the sensitivity of the ISO population to the metallicity-dependence relationship in M. J. Hopkins et al. (2023); that work's Section 4.2 showed that if there were no metallicity dependence, more high-f_{H_2O} ISOs would be present.

To link the velocity distribution of ISOs to that of stars, the following points of dynamics need to be considered. First, we should expect the ISO velocity distribution to have the same pattern of gaps and overdensities as the stellar velocity distribution, without any assumptions about their origins. As discussed in the Introduction (Section 1), the structures in the stellar velocity distribution are caused by resonances with the spiral arms and bar, compared to which individual ISOs and stars both have negligible mass. This means the Galactic orbits of ISOs will be affected by these resonances to the same extent as the orbits of stars. These structures are being actively formed, and since the potentials which cause these resonances are transient with a timescale of ~100 Myr (J. Baba 2015), the velocity distribution structure must form on this timescale or less. This is significantly less than the average age of stars and ISOs in the solar neighborhood, thus the ISO velocity distribution must develop the same pattern of gaps and overdensities as the stellar velocity distribution, regardless of their initial velocity distribution.

Second, ISOs do not stay near their parent stars. The vast majority of stars in the solar neighborhood belong to the Milky Way disk, and so are on near-circular orbits around the Galactic center with an orbital speed of ~200 km s^{-1} (J. Bovy et al. 2012). All significant mechanisms to eject planetesimals from their parent planetary systems produce ISOs with ejection velocities significantly less than this orbital velocity (<10 km s^{-1}; T. O. Hands et al. 2019; S. Pfalzner et al. 2021), therefore ejection puts ISOs onto similar orbits to their parent stars. However, these small differences in velocity mean that ISOs do not stay near their parent star, quickly dispersing along this shared near-circular orbit azimuthally. This means that most of the ISOs we discover passing through the inner solar system do not have parent stars in the immediate solar neighborhood, nor in our Gaia stellar sample.

Regardless, we can still predict the solar neighborhood ISO distribution from the solar neighborhood stellar distribution, because due to their velocity dispersion stars mix azimuthally too.[5] Under the assumption that the Galaxy does not have large deviations from axisymmetry, the distribution of the whole ISO population will follow the distribution of the whole population of stars. Since stars and ISOs are equally negligible in mass compared to the spiral arms, bar, and giant molecular clouds (B. Gustafsson et al. 2016) that dominate the evolution of their orbits, the orbits of ISOs still evolve in the same way as those of stars.[6]

In summary, though individual ISOs do not stay near their own parent stars, the distribution of the whole ISO population follows the distribution of the whole stellar population. Applying the metallicity dependence detailed above gives

$$n_{\rm ISO}(\boldsymbol{x}, \boldsymbol{v}, \tau, f_{H_2O})\, {\rm d}f_{H_2O} \propto 10^{[M/H]} \cdot n_{\rm stars}(\boldsymbol{x}, \boldsymbol{v}, \tau, [M/H])\, d[M/H], \quad (1)$$

where $n_{\rm ISO}$ and $n_{\rm stars}$ are the number density distributions of ISOs and stars, respectively, in position $\boldsymbol{x}$, velocity $\boldsymbol{v} = (U, V, W)$, age τ, and composition as measured by [M/H] for stars and f_{H_2O} for ISOs. f_{H_2O} and [M/H] are linked by the one-to-one relation discussed above, and we treat these distributions as being constant in $\boldsymbol{x}$ over our solar neighborhood sample and focus on the other variables.

We expect the vast majority of ISOs to be released within several hundred million years of a star's formation (S. Pfalzner & M. T. Bannister 2019; C. M. Lisse et al. 2022; A. Fitzsimmons et al. 2023). Since this is significantly less than the average age of stars in the solar neighborhood, we do not account for a substantial delay between a star's birth and the

[5] This is very well demonstrated by the video showing the orbits of a selection of stars from the Gaia Catalog of Nearby Stars at https://www.cosmos.esa.int/web/gaia/edr3-gcns, or equivalently Figure 21 of Gaia Collaboration et al. (2021).

[6] Note, close encounters with individual stars do not contribute to the evolution of the orbits of either stars or ISOs as these are incredibly rare: Stars and ISOs will undergo the same rate of close encounters with individual stars, and the timescale for an object with a speed of 55 km s^{-1} undergoing a 5 au-separation encounter with stars of density 0.1 pc^{-3} is 10^5 Gyr. For a population of age ~10 Gyr, we would expect only 0.01% of ISOs (and stars) to have undergone such a close encounter.

release of its ISOs. Finally, we expect ISOs to outlive their parent stars (see Section 2.1).

The stars in the observed Gaia subsample with measured velocity, metallicity, and age can be thought of as a biased sampling from the chemodynamical distribution shared by both stars and ISOs. Just as weighting these samples by the inverse of the ESF debiases the sample and gives us a prediction of the sine morte stellar distribution, to predict the distribution of ISOs in the solar neighborhood we reweight these samples by the additional ISO production factor of $10^{[M/H]}$, following Equation (1). This distribution is plotted in Figure B1 in Appendix B. The distribution of ISOs in the solar neighborhood however is not the distribution of ISOs that is observable from our place in the inner solar system.

2.4. Within the Solar System: The Volume Sampling Rate and Gravitational Focussing

ISO-detecting surveys such as Pan-STARRS (K. C. Chambers et al. 2016) and LSST have runtimes significantly longer than the typical lengths of time ISOs are visible: 1I and 2I spent only 2 months and 3 yr, respectively, brighter than 24 mag, the LSST single-exposure r-band point-source depth (Ž. Ivezić et al. 2019). Thus the population of ISOs observable at any time is constantly being refreshed. This refreshing effect (previously discussed in S. A. Stern 1990 and A. Moro-Martìn et al. 2009) means that the distribution of ISOs that are observable is the distribution of those streaming through the inner solar system, not the distribution of the static population in the solar neighborhood of Section 2.3. This streaming population experiences two velocity-dependent effects that change their distribution in parameter space relative to the static population. First is the dependence of this refresh rate on relative speed $v_\infty = \sqrt{U^2 + V^2 + W^2}$: for the same spatial density, the observable volume samples ISOs with high v_∞ at a proportionally higher rate. The second effect is gravitational focusing: the increase of the cross section σ at low v_∞ for encounters with ISOs with perihelion less than q (F. L. Whipple 1975; D. Seligman & G. Laughlin 2018; J. C. Forbes & A. Loeb 2019).[7]

These effects are combined in the volume sampling rate:

$$\gamma(q, v_\infty) = v_\infty \sigma = v_\infty \pi q^2 \left(1 + \frac{2GM_\odot}{q v_\infty^2}\right). \quad (2)$$

This follows from classical dynamics and is first referenced in Equation (5) of F. L. Whipple (1975). The volume sampling rate is plotted in Figure 2, scaled by $1/\pi q^2$, the inverse of the geometric cross section. Multiplying the velocity distribution of ISOs in the solar neighborhood by $\gamma(q, v_\infty)$ gives the rate of ISOs with perihelion less than q entering the inner solar system.

Though the volume sampling rate becomes proportional to v_∞^{-1} at low speeds, it is unnecessary to apply a cutoff or gravitational softening. This is because the velocity distribution remains integrable due to the v_∞^2 Jacobian factor that arises from the velocity distribution being three-dimensional. Thus the one-dimensional speed distribution (Figure 3, Speed) becomes proportional to v_∞ at small speeds, and does not diverge. We find adding a gravitational softening parameter $\phi = 2\,\mathrm{km\,s^{-1}}$ (as defined in D. Seligman & G. Laughlin 2018) does not change the likelihoods calculated in Section 4.2.

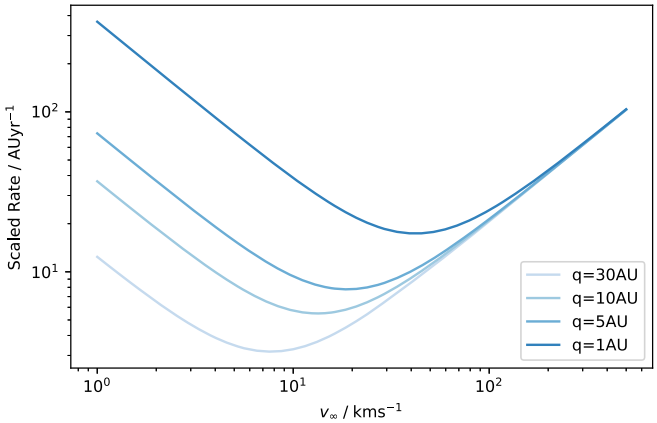

Figure 2. Volume sampling rate scaled by $1/\pi q^2$ for different perihelia q. This is the combination of gravitational focusing, which increases the sampling rate of low-relative-speed ISOs, and the "refresh rate" effect, where faster ISOs are sampled at proportionally higher rates.

To predict the distribution of ISOs entering the inner solar system, we reweight the solar neighborhood ISO distribution described in Section 2.3 by the volume sampling rate for a given q, here $q = 5$ au. The weights applied to the raw Gaia samples to get each distribution are summarized in Table 1.

2.5. Known Objects

Our comparison sample is the two currently known macroscopic ISOs: 1I/'Oumuamua and 2I/Borisov.[8] Objects within the solar system are defined as interstellar based on their orbital energy. Fitting to measured astrometry gives the derived value of the original reciprocal of the semimajor axis at a given distance from the Sun, $1/a_{\rm ori}$, which must be dominantly negative to be hyperbolic (giving an eccentricity $e \gg 1$). This gives the asymptotic speed or velocity at infinity, $v_\infty = \sqrt{U^2 + V^2 + W^2}$: the speed of an ISO on its hyperbolic orbit relative to the Sun before entering the solar system. Both known ISOs were measured for sufficiently long arcs, and relative to Gaia-level stellar catalogs, that the precision of their original orbits is well constrained. We use the barycentric original orbit at a distance of 250 au from the Sun of C. A. L. Bailer-Jones et al. (2018) and C. A. L. Bailer-Jones et al. (2020) for 1I and 2I. It is possible that M. Królikowska & L. Dones's (2023) recent finding of NG acceleration in pre-perihelion comets at $r_h > 5$ au may mean a future revision of 2I's original orbit, and introduces some degree of uncertainty to 1I/'Oumuamua's original orbit; this seems relatively unlikely at present, given the variations in NG accelerations tested by various authors.[9] Unlike 2I, 1I/'Oumuamua's orbit was not precovered into pre-perihelion observations, so only its post-perihelion NG accelerations are quantified (M. Micheli et al. 2018). Nevertheless, the known velocities of both ISOs are uncertain only to tens of meters per second, with the speed and direction changing by factors of only 1 in 1000 both between

[7] This treatment of gravitational focusing differs from that of the *probabilistic method* of D. Marčeta (2023), who calculates the effect on the distribution of ISOs within the solar system at a single moment in time, as opposed to the streaming population.

[8] While the prospect of interstellar meteor detection has been long-standing for many decades, we rely on the assessment of P. G. Brown & J. Borovička (2023) that no interstellar meteoroids are yet confirmed.

[9] For example, Table 1 in both C. A. L. Bailer-Jones et al. (2018, 2020), respectively; also P. A. Dybczyński & M. Królikowska (2018), P. A. Dybczyński et al. (2019), and M. Micheli et al. (2018).

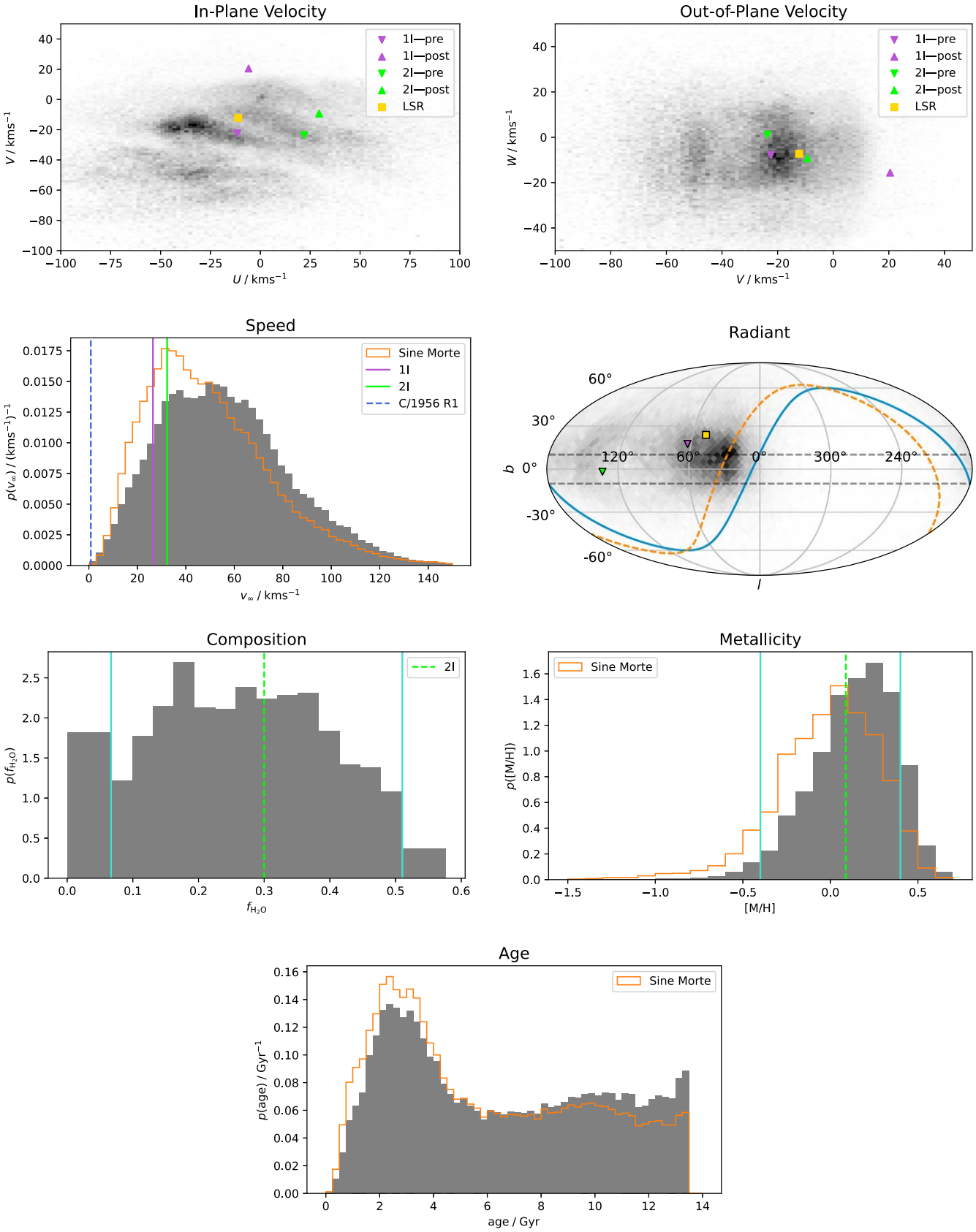

Figure 3. Predicted distributions of ISOs with $q < 5$ au in velocity, on-sky radiant, composition proxied by water mass fraction f_{H_2O}, parent-star metallicity, and age, analogous to Figure 1. On the radiant plot the ecliptic plane is marked in solid blue, the celestial equator is marked in dashed orange, and dashed horizontal lines encapsulate the $b = \pm 10^\circ$ region of high stellar density along the Galactic plane. Orange unfilled histograms plot the distribution of the sine morte stellar population for comparison.

Table 1
Summary of Weights Given to Observed Gaia Data Points to Reconstruct the Stellar and ISO Distributions Used

Distribution	Raw Gaia Samples	Sine Morte Stars	Solar Neighborhood ISOs	$q < 5$ au ISOs
Weight	1	$\frac{1}{\mathrm{ESF}}$	$\frac{10^{[\mathrm{M/H}]}}{\mathrm{ESF}}$	$\frac{10^{[\mathrm{M/H}]}\gamma(5\,\mathrm{au}, v_\infty)}{\mathrm{ESF}}$

Note. The effective selection function (ESF) is a function of each Gaia sample's distance, age, metallicity, and on-sky position.

NG acceleration models and within the uncertainties of each model—and it is the velocities that are the key parameter for our analysis here. For the post-encounter asymptotic velocity, we use the full observed arc orbits of JPL Horizons.[10]

Some solar system comets have been considered as potential marginal cases of ISOs, often with weakly hyperbolic $e \sim 1.01$–1.05. For reference, of our distributions against such long-period comets, we use as an example the bright comet C/1956 R1 (Arend-Roland), which was at one time considered as potentially the first interstellar comet (Z. Sekanina 1968). It has a 497 days arc (with astrometry measured relative to non-Gaia-calibrated photographic plates), and is among a small group of comets with a high N_2/CO_2 production ratio (S. E. Anderson et al. 2023).

3. Results

3.1. Interstellar Object Distribution

Plotted in Figure 3 is the predicted distribution of $q \leqslant 5$ au ISOs entering the solar system in two-dimensional velocity, speed, on-sky radiant, composition, source stellar metallicity, and age.

We first consider the velocity distribution of ISOs in their Cartesian components U, V, and W in two two-dimensional histograms (Figure 3, In-Plane Velocity and Out-of-Plane Velocity). As expected given that stars are the progenitors, under our model in Section 2.3 the ISO velocity distribution shows the same moving groups and branches as the stellar distribution of Figure 1. Many ISOs will have pre-encounter velocities in these structures: We predict 18% of ISOs passing through the inner solar system will originate in the largest of these, the Hyades-Pleiades branch.[11] However, the ISOs display an additional peak at the Sun's velocity (U, V, $W = 0$, 0, 0) when compared to the stellar distribution due to gravitational focusing, discussed in Section 2.4 and illustrated in Figure 2. We use a $q \leqslant 5$ au cut as indicative, for example for ease of observational characterization, as typical of solar system comets. For comparison, the resulting ISO distributions with q cuts instead made at 1 au and at 30 au are shown in Appendix B. The solar velocity concentration becomes more pronounced as the perihelion cut decreases, as expected; by $q = 30$ au, there is effectively no gravitational focusing. As in Figure 1, we mark with a yellow square the LSR (R. Schönrich et al. 2010), the indicative velocity of a star on a circular orbit in a theoretical azimuthally smoothed Galactic potential.

To compare this predicted population with the known sample of detected ISOs, we indicate in Figure 3 the Cartesian component velocities of 1I/'Oumuamua and 2I/Borisov both before and after their perturbing interaction with the solar system (Section 2.5); 1I is marked in purple and 2I in green. The pre-encounter velocities are directly comparable to our predicted population; the post-encounter velocities are to illustrate the effects of the only two measured ISO gravitational interactions with the Sun. Both known ISOs' pre-encounter velocities are entirely typical for the population, occurring in regions of velocity space with relative ISO abundance. This places both ISOs within moving groups in velocity space; we discuss the implications of this in Section 4.1.

We next consider the asymptotic speed v_∞ distribution of ISOs (Figure 3, Speed). This asymptotic speed distribution is similar to that predicted by T. M. Eubanks et al. (2021), but weighted higher, with our median asymptotic speed being 55 km s^{-1}, compared to their 38 km s^{-1}. This is largely due to our choice in these plots of calculating gravitational focusing for $q < 5$ au rather than T. M. Eubanks et al.'s (2021) $q < 1$ au, which places less weighting on low-speed ISOs. When we calculate the speed distribution for $q < 1$ au (Figure B2, Speed) we get a median speed of 45 km s^{-1}. For large perihelia the effect of gravitational focusing becomes negligible (e.g., for $q < 30$ au ISOs, plotted in Figure B3, Speed). The remaining difference may be due to the metallicity dependence of ISO production that we assume. We mark the asymptotic speeds of 1I, 2I, and example solar system comet C/1956 R1 (Section 2.5) on Figure 3. Again, the two known ISOs are entirely typical relative to this distribution. Our predicted distribution gives a p-value of 10^{-5} for an ISO having a speed relative to the Sun lower than that of the weakly hyperbolic C/1956 R1—making this comet's solar system origin and Oort cloud membership significantly preferred. This reproduces a result of F. L. Whipple (1975), who gave an analytic expression for this probability assuming a Gaussian velocity distribution, and determined C/1956 R1 to have a p-value in the range 2×10^{-7}–1×10^{-4}.

The three-dimensional velocity distribution combined with the Sun's motion generates a projected distribution of the velocities of ISOs on the sky. The radiant is the direction of approach of an ISO on its way into the solar system, and is equal to the angular direction of its velocity vector relative to the Sun. This is plotted in Galactic longitude and latitude l and b in Figure 3 (Radiant). Due to the motion of the Sun relative to the LSR, the predicted radiant distribution clusters near the solar apex, marked here by the same yellow square, as expected (e.g., T. A. McGlynn & R. D. Chapman 1989; S. A. Stern 1990; D. Seligman & G. Laughlin 2018). Since gravitational focusing increases in an isotropic manner the rate of ISOs entering the inner solar system that have velocities similar to that of the Sun, it has the effect of increasing the proportion of ISOs with radiants not near the apex, diluting the peak. In this projection the moving groups are not as easily apparent, because they are effectively in a linear clump from our point of view.

We can now consider the physical properties of the ISOs themselves. Here our example property, after M. J. Hopkins

[10] Solar System Dynamics (downloaded 2023 December 20). 1I: https://ssd.jpl.nasa.gov/tools/sbdb_lookup.html#/?sstr=1I, solution as of 2018 June 26 12:17:57; 2I: https://ssd.jpl.nasa.gov/tools/sbdb_lookup.html#/?sstr=2I, solution as of 2020 August 21 09:32:58.

[11] Defined here with boundaries $V < -5$ km s^{-1}, $U > -55$ km s^{-1}, $V > -35$ km s^{-1} $-0.2U$, and $V < -25$ km s^{-1} $-0.6U$, following Figure 5 of T. Antoja et al. (2008).

et al. (2023), is the ISO water mass fraction. It should be noted that this distribution is for ISOs which formed outside the water-ice line only, however, as discussed in Section 2.3, we expect this to be true for most ISOs. The distribution of water mass fraction of the ISOs entering the inner solar system within the range of the B. Bitsch & C. Battistini (2020) chemical model is shown in Figure 3 (Composition). The overall distribution is broad. For reference, the inferred water mass fraction of 2I/Borisov, the only ISO with this property somewhat constrained from production rates, is marked by a vertical green line (D. Z. Seligman et al. 2022). We discuss composition further in Section 3.2.

The age distribution of ISOs entering the inner solar system (Figure 3, Age) is very similar to that of the sine morte stellar population. There are a couple of effects which could cause these to differ, however neither end up having a large effect. First, stars are observed to show a correlation between their ages and velocity dispersions (e.g., B. Nordström et al. 2004) and a similar correlation in ISOs would cause older, faster-moving ISOs to cross the solar system more often, be more highly weighted by the volume sample rate (Equation (2)), and shift the ISO distribution toward higher ages. This does occur and can be seen in Figure B1 (Age), though the effect is small. Second, as discussed in Section 2.2, the solar neighborhood has a flat age–metallicity relation, meaning that even if ISO production correlates with metallicity as we assume, there are high-metallicity, high-ISO-production stars at all ages and the ISO and stellar age distributions will remain very similar. ISOs of all ages are passing through the solar system: While there is a peak at 3 Gyr, we predict the ISO age distribution will be sampled quite evenly from stars across the age of the Galaxy.

Finally, we also include the distribution of the metallicities of the parent stars of the ISOs entering the inner solar system (Figure 3, Metallicity). This tends toward higher metallicities than the overall stellar distribution. This outcome is due to the metallicity dependence that we apply to our ISO production (Section 2.3): Since in our model higher-[M/H] stars produce more ISOs, more ISOs come from higher-[M/H] stars. On this distribution we have plotted the value of [M/H] corresponding to 2I's water mass fraction of 0.3, showing that for this physical property value, 2I would have come in our model from a star of metallicity [M/H] ≈ 0.1.

We can also now see the stellar origin of the ISOs on either side of the range of the planetesimal-composition model. Though we cannot measure the distribution of ISOs in f_{H_2O} outside of the boundaries of the chemical model (marked by vertical turquoise lines), we can still quantify the fraction of ISOs on either side. We show the contribution to the distribution below the range in a bin covering 0 to the lower limit ($f_{H_2O} = 0.07$), and above the range in a bin of the same width. The bin above the range of the chemical model has a low density, showing the f_{H_2O} distribution only extends a little above the range that we can measure. On the other hand, the bin below the lower limit of the chemical model has a high density, meaning the composition distribution must have a second peak in this bin, even if it is outside of the range where we can model it. A tiny number of ISOs come from stars with metallicities below the lower limit, whereas a more significant number come from stars with metallicities above the upper limit. In our model, extremely metal-poor stars contribute almost no ISOs to the solar system neighborhood.

3.2. Chemodynamics

Stars in the Milky Way exhibit correlations between composition and dynamics, so we expect ISOs with varied compositions to also have different velocity and age distributions. Milky Way stars are loosely grouped into a high-metallicity, low-velocity-dispersion, low-age "thin disk" and a low-metallicity, high-velocity-dispersion, high-age "thick disk" (A. Recio-Blanco et al. 2014). To explore these correlations in the ISO population, we split our predicted ISO distribution in half by water mass fraction, relative to the median $f_{H_2O} = 0.25$. Again, this applies only to ISOs formed outside the water-ice line, but we expect this to be true for most ISOs. For ease of reading, we term these two groups "sandy" ($f_{H_2O} < 0.25$) and "frosty" ($f_{H_2O} > 0.25$).[12]

Since ISO water mass fraction decreases monotonically with parent-star metallicity, frosty ISOs originate from *low*-metallicity stars, with [M/H] < 0.16, and sandy ISOs originate from *high*-metallicity stars, with [M/H] > 0.16. For example, 2I would fall in the $f_{H_2O} > 0.25$ frosty group. The plots in Figure 4 show the fraction of ISOs at each velocity, radiant, and age that are sandy. Notably sandy ISOs, like the high-metallicity stars they originate from, are preferentially found in the moving groups (compare Figures 3 and 4, In-Plane Velocity) with the sandy ISO fraction greater than 0.5 signifying that they make up the majority.

Conversely, frosty ISOs are much more continuously distributed, and are in the majority at higher speeds relative to the Sun. This difference is most clear in the radiant plot, which shows that the majority of ISOs entering the inner solar system near the solar apex will be sandy, whereas ISOs on other trajectories will be predominately frosty. Additionally, the age distribution changes between the two populations, with the sandy distribution being weighted toward older ISOs than the frosty population. This is a product of the presence of old high-metallicity stars in the solar neighborhood (see Figure 1, Age–Metallicity). Less notably, both sandy and frosty ISOs are found at all values of v_∞, with a slight preference for frosty ISOs at higher speeds.

4. Discussion

The correlations we show in Section 3 in our chemodynamical distribution mean that substantial information about the origin of an ISO can be inferred from its velocity alone. The conditional distribution of ISO compositions, parent-star metallicities, and ages depends on the given velocity. That is, even if we only know the velocity of an ISO, we can still calculate the probability distribution its composition, parent-star metallicity, and age must have been drawn from. These correlations will allow us to make inferences about partially characterized ISOs found in future surveys. Our approach could also be used to constrain the origin of more exotic planetesimal ISOs found in the future: If an object were not described well by our current chemical model, e.g., an icy fractal aggregate (A. Moro-Martìn 2019), we can still use our distribution to constrain the metallicity of its home star.

Velocity is one of the first parameters that can be measured for a newfound minor planet: For an ISO, with its comparatively high velocity relative to solar system objects, it is quantifiable with a relatively short orbital arc, e.g.,

[12] Purely compositional: no descriptor of comae grain size is implied.

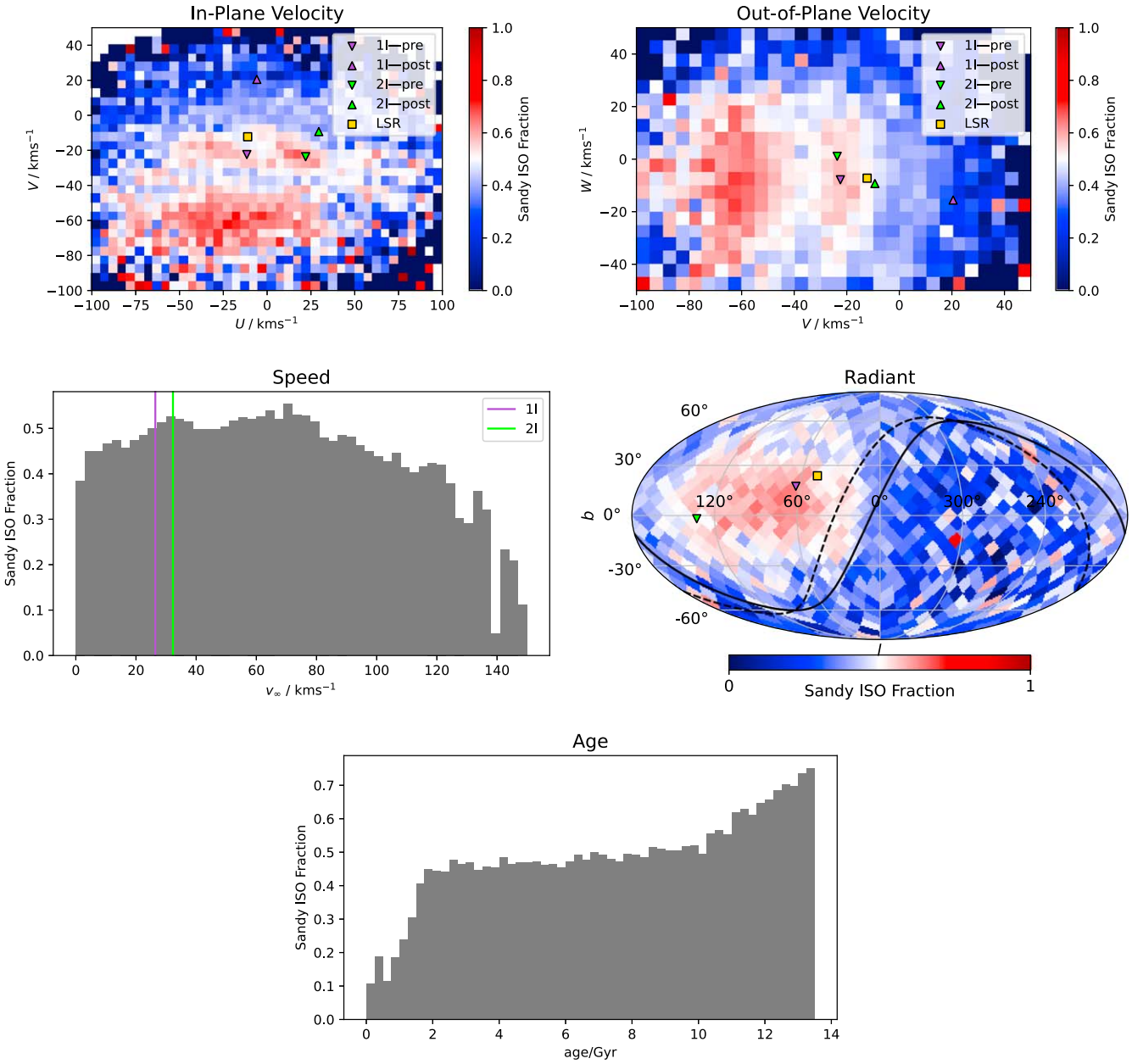

Figure 4. Fraction of $q < 5$ au ISOs at each velocity, radiant, and age that are "sandy" ($f_{\rm H_2O} < 0.25$). Sandy ISOs form the majority in moving groups and low V, and at higher ages.

4–7 days for LSST (N. V. Cook et al. 2016). Until then, orbital solutions have not yet settled, and new discoveries often sit at marginally hyperbolic ($e \sim 1.01$–1.03). The Gaia-based v_∞ distribution we present in Figure 3 can be used for testing both future ISO discoveries and known solar system comets that have been hypothesized to have interstellar origins (e.g., C/1956 R1). From Figure 3, the uncertainties on the velocities of discovered ISOs will need to be $\lesssim$5 km s^{-1} for their velocity distribution identification to be crisp, as this is approximately the scale of the moving groups.

Perhaps the most striking feature of our results is that local ISOs are indeed coming from stars of all ages in the Galaxy. This wide age distribution is a natural outcome, given the wide stellar age distribution and the fact that ISOs outlast stars. This is due to radial migration; stars currently in the solar neighborhood have origins over a large range in Galactic radius (J. A. Sellwood & J. J. Binney 2002; J. Lian et al. 2022). Stars mix even faster azimuthally, as discussed in Section 2.3. This means stars that happen to currently be nearby have in fact been sourced from all over the Galactic disk.

The result is that the population of stars and therefore ISOs currently near the Sun at any particular velocity is a dynamic mix of many different populations, sourced from all ages and a large swath of the disk. There are correlations, as the population is not fully mixed. For instance, younger stars which have more circular orbits are more affected by resonances (K. J. Daniel & R. F. G. Wyse 2015), and so end up in moving groups more frequently. This however equally applies to the abundant population of low-velocity old stars. Unlike in purely stellar studies, ISOs have the potential for ground truth by spacecraft visits, such as Comet Interceptor (G. H. Jones et al. 2024), together with remote telescope

observation. Our prediction of the broad age spread of ISOs would be testable with detailed isotopic ratios and compositions, from comae or sample return missions.

4.1. Implications for the Two Known ISOs

The pre-encounter velocities of 1I and 2I in Figure 3 both lie within the boundaries of particular overdensities in velocity space. We reiterate that although overdensities in velocity space were originally thought to be from dispersed, coeval stellar clusters, it is now thought that they are caused by resonances with the Galaxy's transient spiral arms and bar clearing gaps in the *U*–*V* plane (J. Skuljan et al. 1999). This is supported by the kiloparsec-scale extent that some of these overdensities display (P. Ramos et al. 2018).

For 1I/'Oumuamua, this overdensity is called the Pleiades moving group (J. Zhao et al. 2009), part of the Hyades-Pleiades branch (J. Skuljan et al. 1999), named after the Pleiades open cluster (M45) that it contains. The Pleiades *moving group* is distinct from the Pleiades *open cluster*, so to avoid confusion we use the te reo Māori name for the open cluster: Matariki (R. Mātāmua 2020). Though S. Lucchini et al. (2023) show that the Pleiades moving group has a comparatively small radial extent among moving groups, the age distribution of its members is noncoeval (T. Antoja et al. 2008): This crucial point means that the moving group is far more than just the dispersal of Matariki. Additionally, J. Heyl et al. (2022) counts only ~1500 members of Matariki including escapees, but S. Lucchini et al. (2023) find ~150,000 stars belonging to the Pleiades moving group. We emphasize this distinction because 1I/'Oumuamua's membership is of the Pleiades moving group; this does not imply formation around a star in Matariki, or at a star of one of the other young stellar associations that happen to be currently nearby (e.g F. Feng & H. R. A. Jones 2018) and are in the moving group.

1I/'Oumuamua's pre-encounter velocity is also relatively near the LSR, with approximately 2% of our predicted ISO distribution having a velocity closer to the LSR. However, Figure 3 (In-Plane Velocity) shows that the exact velocity of the LSR is not a preferred point in the local velocity distribution. In particular, the structure of the branches means there is a natural gap between the LSR and 1I/'Oumuamua's velocity. It is therefore not appropriate to attribute significance to the proximity of 1I to the LSR as though the velocity distribution were a Gaussian centered on the LSR. We predict that as the sample of known ISOs increases, until 50 ISOs are known, it is most likely that 1I/'Oumuamua will remain the closest to the LSR. This is a natural outcome of the inherently clumpy distribution.

2I/Borisov was in the Coma Berenices moving group (see Figure 5 of T. Antoja et al. 2008) before its solar encounter. This moving group is named after, though is distinct from, the constellation Coma Berenices. Similarly, it does not represent the origin of 2I, only a transient location in velocity space caused by the clearing of the gaps by transient spiral and bar potentials.

We can use the correlations of an ISO's other properties with velocity to make inferences about the distributions that an ISO's composition, parent-star metallicity, and age must be drawn from. For ISOs discovered in the future, this means inferences can be made about their other properties based only on their velocity, which is easiest to constrain. Here we explore what can be inferred about 1I and 2I based only on their velocities. We do this by evaluating the composition, parent-star metallicity, and age distribution of 1I and 2I using only observed Gaia stars with velocities within $5\,\mathrm{km\,s^{-1}}$ of each ISO's pre-encounter velocity; these are plotted in Figure 5. Setting $5\,\mathrm{km\,s^{-1}}$ is a relatively arbitrary bound that provides a suitably large restricted sample (793 observed stars for 1I and 255 observed stars for 2I); since it is smaller than the overall sample, to ensure the differences in the histograms are significant, we calculate error bars for the value of the distribution in each bin. As this is a weighted sum, the variance of each value is equal to the sum of the squared weights in each bin. Our approach uses the actual measured age and metallicity distributions of stars at the velocities of interest, but is otherwise similar to the approach used by F. Almeida-Fernandes & H. J. Rocha-Pinto (2018), who inferred a confidence interval on the age of 1I from its velocity using a model of the stellar age–velocity correlation. They estimate 1I's age as 200 Myr–450 Myr. However, their analysis uses a smooth Gaussian distribution for the stellar velocity distribution, which Figure 3 shows is not representative, and their result is also dependent on the model used for the age–velocity relation. On the validity of our own age distribution, we note that measuring ages with isochrone fitting (like Gaia's FLAME pipeline) can be prone to bias (B. Nordström et al. 2004), though, as noted in Section 2.1, in comparison to literature ages M. Fouesneau et al. (2023) finds FLAME ages to have mean biases and dispersions of only 0.1–0.3 Gyr and 0.25 Gyr, respectively. Additionally, our distributions in Figure 5 are from samples with a large extent in space (a sphere of radius 200 pc). In future, more accurate predictions of the known ISOs' distributions could be achieved by using observed stars with both similar velocity and position.

We find that at the velocities of both 1I and 2I there are ISOs with a wide range of ages and compositions, and the distributions for both generally follow those of the overall population. This is due to the mixing described above: At any particular velocity there are stars with a wide range of ages and metallicities. However, the correlations with velocity cause some notable differences. Chemically, the distributions for both ISOs are shifted toward lower $f_{\mathrm{H_2O}}$ and higher parent-star metallicities. In age, the distribution for both ISOs is broad, but 1I is shifted toward lower values, and 2I toward higher values. This is expected from the relative speeds of 1I and 2I to the LSR given that younger stars have generally lower velocity dispersions than older, but it is important to note that stars of all ages can be found at the velocities of both ISOs. This is backed up by previous studies showing that the Pleiades moving group is made up of stars of all Galactic ages (T. Antoja et al. 2008; B. Famaey et al. 2008). Thus these results suggest that 1I is not necessarily young.

4.2. Predictions and Model Testing by Future Surveys Such as LSST

It is currently unknown how many ISOs Rubin's LSST will detect; the theoretical predictions are at a nascent state. Estimates have varied by orders of magnitude, spanning ones, tens, and hundreds (e.g., A. Moro-Martìn et al. 2009; N. V. Cook et al. 2016; D. Marčeta & D. Z. Seligman 2023). However, two points are clear: the single-image depth increase by 3 orders of magnitude over previous surveys (e.g., Pan-STARRS, K. C. Chambers et al. 2016) will dramatically improve the detectable parameter space for ISOs; and the first 2

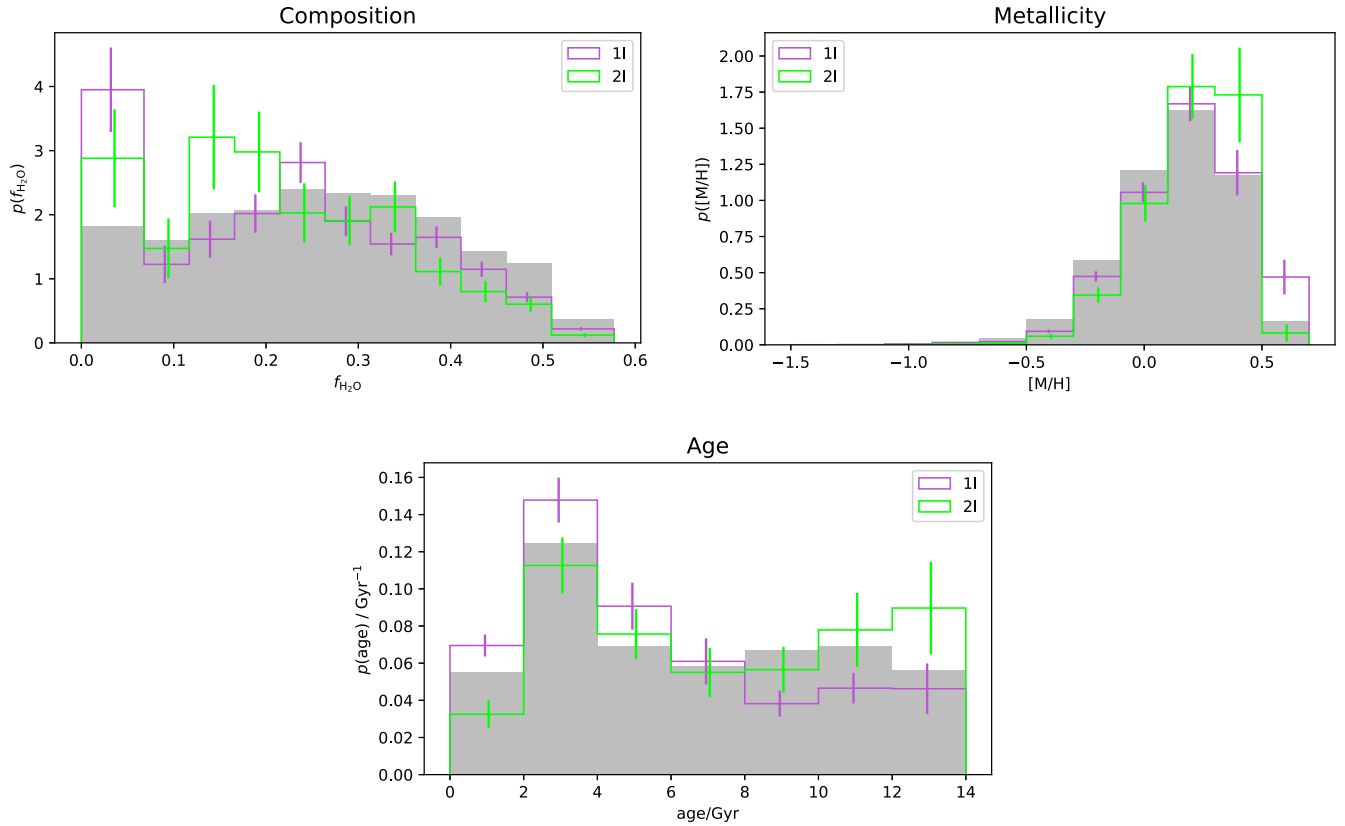

Figure 5. Predicted distribution of ISOs with similar velocities to 1I and 2I in composition, age, and [M/H]. For comparison, the overall ISO population distribution in Figure 3 is also shown, in gray.

yr of surveying will scan the solar volume to initial completeness, until the rapid motion of ISOs refreshes. Clearly, nuanced theoretical models are critical for building toward improved detection estimates.

With a major survey on the way that is expected to increase the sample size of ISOs considerably beyond the current two, we assess what number of ISOs would be needed to distinguish between models of the velocity distribution. Note that we are not yet incorporating the actual on-sky performance of LSST or any other survey; surveys provide actual detections with a complex efficiency function. Also, our approach here does not provide an absolute spatial number density of ISOs; we defer this to future work. Here we purely make a prediction of the number of ISOs needed to distinguish models. As discussed in Section 1, the velocity distribution of ISOs in the solar neighborhood has most frequently been assumed to be a smooth multivariate Gaussian. We calculate the number of ISOs we would need in order to distinguish the realistic, featured velocity distribution we predict from a smooth Gaussian. As described in M. J. Hopkins et al. (2023), a predicted distribution of ISOs can be used as a likelihood function to perform inference. The likelihood function for a Gaussian velocity distribution with a volume sampling rate included is simply the product of the Gaussian probability density function and the volume sampling rate, normalized. We estimate the likelihood function of our Gaia model with a k-nearest neighbors (kNN) method, based on that of P. Zhao & L. Lai (2020): For each sample velocity we sum the normalized ISO weights of the 99 nearest neighbor points in our Gaia distribution, divided by the volume of a sphere in velocity space with radius out to the 100th nearest neighbor. For reference, slices though the resulting likelihood function are shown in Appendix C (Figure C1).

When a survey such as Pan-STARRS or LSST finds a sample of ISOs, the likelihood of different models producing the observed velocity distribution can be calculated and compared to determine the more likely model. Here we calculate the number of ISOs that will be required to discriminate between different models, for each of a series of models: our Gaia model, and the Schwarzschild velocity distributions fit to M-, G- and OB-type giant stars used by D. J. Hoover et al. (2022) and D. Marčeta (2023).[13] We draw samples of different sizes N from each model velocity distribution, then calculate the log likelihood of each sample being drawn from each other model. Repeating this with new samples, we calculate the mean and standard deviation of the log likelihoods of each pair of models. We can then calculate the significance of each distinction for each sample size N; these are all listed in Table 2. This is equivalent to a series of relative likelihood tests (H. Akaike 1974).

Positing that the true distribution of ISOs is what we have predicted here using Gaia, we focus on the sigma values of the Gaia model samples relative to the other models. We find that at $N = 50$, a 3σ discrepancy is detectable to the OB-type Schwarzschild distribution. This is because this distribution has the lowest velocity dispersions, far lower than those of the overall stellar population, making it the most different to our

[13] The Schwarzschild distribution is a multivariate Gaussian inclined in the U–V plane by a vertex deviation l_v; the parameters used by D. J. Hoover et al. (2022) and D. Marčeta (2023) are listed in Table 10.3 of J. Binney & M. Merrifield (1998), copied from J. Delhaye (1965) but ultimately sourced from P. P. Parenago (1951).

Table 2
Details of Distinguishing Models

Sample Size	Sample Model	Mean ± Std of Log Likelihood with Model				Significance Relative to Sample Model (σ)			
		Gaia	M	G	OB	Gaia	M	G	OB
$N = 50$	Gaia	-14.0 ± 0.2	-14.4 ± 0.4	-14.9 ± 0.7	-21.8 ± 2.2	**0.0**	**0.7**	**1.3**	**3.5**
$N = 50$	M	-14.0 ± 0.1	-13.8 ± 0.2	-14.0 ± 0.3	-18.5 ± 1.1	0.8	0.0	0.8	4.4
$N = 50$	G	-13.6 ± 0.1	-13.4 ± 0.1	-13.3 ± 0.2	-15.6 ± 0.7	1.6	0.8	0.0	3.2
$N = 50$	OB	-12.9 ± 0.1	-12.7 ± 0.0	-12.2 ± 0.1	-11.4 ± 0.2	7.8	7.6	4.7	0.0
$N = 100$	Gaia	-14.0 ± 0.1	-14.3 ± 0.3	-14.9 ± 0.4	-21.5 ± 1.4	**0.0**	**1.0**	**1.9**	**5.2**
$N = 100$	M	-14.0 ± 0.1	-13.8 ± 0.1	-14.1 ± 0.2	-18.4 ± 0.7	1.1	0.0	1.2	6.3
$N = 100$	G	-13.6 ± 0.1	-13.4 ± 0.1	-13.3 ± 0.1	-15.6 ± 0.5	2.3	1.1	0.0	4.5
$N = 100$	OB	-12.9 ± 0.1	-12.7 ± 0.0	-12.2 ± 0.0	-11.4 ± 0.1	12.0	11.3	7.1	0.0
$N = 150$	Gaia	-14.0 ± 0.1	-14.4 ± 0.2	-14.9 ± 0.4	-21.6 ± 1.2	**0.0**	**1.2**	**2.2**	**6.2**
$N = 150$	M	-14.0 ± 0.1	-13.8 ± 0.1	-14.0 ± 0.2	-18.4 ± 0.6	1.3	0.0	1.5	8.1
$N = 150$	G	-13.6 ± 0.1	-13.4 ± 0.1	-13.2 ± 0.1	-15.5 ± 0.4	3.2	1.6	0.0	6.0
$N = 150$	OB	-12.9 ± 0.0	-12.7 ± 0.0	-12.2 ± 0.0	-11.4 ± 0.1	15.7	14.7	9.4	0.0

Note. Most relevant is the sigma values of our Gaia model relative to the other models, as this is what we posit as the intrinsic population, so these are marked in bold.

Gaia sample. Dropping the sample to $N = 20$ still reaches a discrepancy of significance 2σ to the OB-type model. At a larger but still reasonable sample size of $N = 100$, the discrepancy between our Gaia sample and the OB-type model exceeds the 5σ level. The G-type model reaches 2σ at $N = 50$. The discrepancy between our Gaia sample and the M-type model is the lowest of the three Schwarzschild models because this model has the largest velocity dispersions, and is the closest match to our Gaia distribution. To reach a 2σ-level discrepancy between the featured Gaia model and the M-type Schwarzschild model, we need a sample size of $N = 350$ ISOs.

This shows that a moderate-scale sample of ISOs, such as expected from LSST following debiasing, will distinguish between velocity models. Indeed, it shows a need for a broad slate of theoretical models exploring the full range of production mechanisms for ISOs, which make testable predictions. Our approach similarly applies to chemodynamic models. We tested an alternate model with no metallicity dependence for ISO production (e.g., M. J. Hopkins et al. 2023 Section 4.2); while that appears physically unlikely, several thousand would be needed before a difference is detectable, as the resulting velocity distributions are very similar.

We suggest that the solar apex should be targeted to improve the detection of inbound ISOs at large heliocentric distances. Our results in Section 3 confirm that while ISOs that will enter the inner solar system will approach from directions all across the sky, more ISOs that will enter the inner solar system will approach from near the solar apex, as demonstrated in Figure 3 (Radiant). Such targets would be particularly suited for spacecraft missions, such as Comet Interceptor, if their Δv and flyby solar aspect angle requirements are met (D. Seligman & G. Laughlin 2018; J. P. Sánchez et al. 2021; G. H. Jones et al. 2024). Figure 3 (Speed) implies a reasonable proportion of the ISO population may be accessible, though we do not compute mission accessibility here. The velocity structures mean ISOs from the moving groups will approach from near the solar apex (Figure 3). Our chemodynamic modeling shows more ISOs from the moving groups are sandy ISOs (Figure 4). However, we note that frosty ISOs still preferentially enter the inner solar system from near the solar apex. Fortunately, half of the region of high ISO radiant density around the solar apex is within LSST's `baseline_v3.3_10yrs` footprint, so we predict that the velocity structures will be detectable by LSST.[14] This region within the footprint of some ~2500 deg^2 is thus suited for an LSST mini-survey. The chemodynamic structures should be detectable but may be more marginal, as they depend both on protoplanetary disk models and on observational characterization subsequent to survey discovery. The water mass fraction variation could produce a range in the level of coma, which would affect initial detectability. While we do not model it here, if the chemodynamic correlation in water mass fraction extends into other volatiles, early detection of inbound frosty ISOs that would enter the inner solar system could be possible in CO-sensitive wavelengths, e.g., with the Atacama Large Millimeter/submillimeter Array or NEO Surveyor.

5. Conclusion

We used chemodynamical measurements of nearby stars with Gaia, accounting for the survey's selection function and stellar death, to build the first high-resolution model of the sine morte stellar population in the solar neighborhood. We then combine this with models of how the Galactic ISO population relates to its parent stellar population, after M. J. Hopkins et al. (2023), and a protoplanetary disk chemical model assuming ISOs are largely sourced from outside the water-ice line. From this, we make a novel prediction of the chemodynamical distribution of the ISOs passing through the solar system.

Our Ōtautahi-Oxford model predicts that the ISO velocity distribution is highly structured into moving groups and branches, like the stellar velocity distribution, and that low-f_{H_2O} ISOs reside mainly in moving groups. This chemodynamic variation also causes a correlation with the radiant, as ISOs approaching the Sun from a direction near the solar apex have lower water mass fractions. Targeting surveying near the solar apex will allow us to detect ISOs on their way into the inner solar system, providing targets for spacecraft missions such as Comet Interceptor. The ISO distributions we predict here can be used to assess the properties of the home stellar population of ISOs within weeks after the ISOs' discovery.

[14] https://community.lsst.org/t/baseline-v3-3-run-released/8042

The current observed ISOs are typical of the predicted population. Both 1I and 2I belong to moving groups that are the transient products of resonances with the Galactic potential. We find that the pre-encounter velocity of 1I/'Oumuamua belongs to the Pleiades moving group (there is no preferred origin in the open cluster Matariki, M45), while 2I/Borisov belongs to the Coma Berenices moving group. 1I/'Oumuamua is typical, rather than unusual—the Hyades-Pleiades branch from which it came will be the source of 18% of the $q < 5$ au ISOs passing through the inner solar system. The correlations between velocity and other properties mean we can use the velocities of the known ISOs to predict the distributions their ages and compositions must have been drawn from. We find that the composition distributions of both 1I and 2I are weighted toward lower values of f_{H_2O} and higher parent-star metallicities compared toward the overall population. The age distribution for 1I is shifted slightly toward younger values and for 2I is shifted toward older values; this is expected from the correlation of stellar velocity dispersion with age. However, we find that both ISOs share their velocities with stars of all ages, so they could have any age.

Finally, we find that in addition to being visually complex and featured, our prediction will be distinguishable from smooth Gaussian velocity distributions, e.g., those fit to M-, G- and OB-type giant stars used by D. J. Hoover et al. (2022) and D. Marčeta (2023). Using relative likelihood tests we calculate that with a sample of 50 ISOs drawn from our predicted distribution, we could rule out the OB-type giant velocity distribution for ISOs to a 3σ level. This significance rises to 5σ with a sample of 100 ISOs. This method can be generalized to compare any model.

Almost all the ISOs we will see will have come to us from across the Galaxy and across cosmic time. The upcoming ISO sample thus holds the possibility of independently testing both the universality of planetesimal formation theories such as the streaming instability, and the current understanding of Galactic star formation history. It will be up to the creation of theoretical models for planetesimal and ISO formation, a more detailed understanding of the nuances of ISO dynamics in the Galaxy, and the exquisite detection capabilities of the surveys of the 2020s and 2030s to bring this promise to reality.

Acknowledgments

We thank John C. Forbes, Rosemary Dorsey, and Joe Masiero for helpful discussions, and Sarah Anderson for the suggestion of comparing C/1956 R1.

M.J.H. acknowledges support from the Science and Technology Facilities Council (STFC) through grant No. ST/W507726/1. M.T.B. appreciates support by the Rutherford Discovery Fellowships from New Zealand Government funding, administered by the Royal Society Te Apārangi.

This work has made use of data from the European Space Agency (ESA) mission Gaia (https://www.cosmos.esa.int/gaia), processed by the Gaia Data Processing and Analysis Consortium (DPAC, https://www.cosmos.esa.int/web/gaia/dpac/consortium). Funding for the DPAC has been provided by national institutions, in particular the institutions participating in the Gaia Multilateral Agreement.

Appendix A
Gaia Archive Queries

For data:

```
SELECT s.parallax AS plx, s.parallax_over_error, s.
  ra AS ra, s.dec AS dec,
s.pmra AS pmra, s.pmdec AS pmdec,s.
  radial_velocity AS rv, s.radial_velocity_error,
ap.mh_gspspec AS mh, apsupp.age_flame_spec, apsupp.
  flags_flame_spec
FROM gaiadr3.gaia_source AS s JOIN gaiadr3.
  astrophysical_parameters AS ap USING (source_id)
JOIN gaiadr3.
  astrophysical_parameters_supp as apsupp USING
  (source_id)
WHERE s.parallax>5 AND s.parallax_over_error>10
AND s.radial_velocity IS NOT NULL AND s.
  radial_velocity_error<5
AND ap.mh_gspspec IS NOT NULL AND apsupp.
  age_flame_spec IS NOT NULL AND apsupp.
  flags_flame_spec='0'
```

For selection function k:

```
SELECT GAIA_HEALPIX_INDEX(2,source_id) AS healpix_,
FLOOR((gs.phot_g_mean_mag - 3)/
  1.0) AS phot_g_mean_mag_, FLOOR((gs.g_rp - -1.0)/
  0.2) AS g_rp_,
COUNT(*) AS k FROM gaiadr3.gaia_source AS gs
JOIN gaiadr3.
  astrophysical_parameters AS ap USING (source_id)
JOIN gaiadr3.
  astrophysical_parameters_supp AS apsupp USING
  (source_id)
WHERE gs.parallax_over_error>10 AND gs.
  radial_velocity_error<5 AND gs.
  radial_velocity IS NOT NULL
AND ap.mh_gspspec IS NOT NULL AND apsupp.
  age_flame_spec IS NOT NULL AND apsupp.
  flags_flame_spec='0'
AND gs.phot_g_mean_mag > 3 AND gs.phot_g_mean_mag < 17
AND gs.g_rp > -1.0 AND gs.
  g_rp < 2.0 GROUP BY healpix_, phot_g_mean_mag_, g_rp_
```

For selection function n:

```
SELECT sq.healpix_, sq.phot_g_mean_mag_, sq.
  g_rp_, COUNT(*) AS n
FROM ( SELECT GAIA_HEALPIX_INDEX(2,
  source_id) AS healpix_,
FLOOR((gs.phot_g_mean_mag - 3)/
  1.0) AS phot_g_mean_mag_,
FLOOR((gs.g_rp - -1.0)/0.2) AS g_rp_ FROM gaiadr3.
  gaia_source AS gs
WHERE gs.phot_g_mean_mag > 3 AND gs.
  phot_g_mean_mag < 17 AND gs.g_rp > -1.0 AND gs.g_rp < 2.0
) AS sq GROUP BY sq.healpix_, sq.
  phot_g_mean_mag_, sq.g_rp_
```

Appendix B
The Effect of the Volume Sampling Rate and Gravitational Focussing

In this appendix, we explore how the ISO distribution depends on the volume sampling rate (Section 2.4). We replot the distributions shown in Figure 3 with different volume sampling rates applied. In Figure B1, we plot the solar neighborhood ISO distribution, with no volume sampling rate

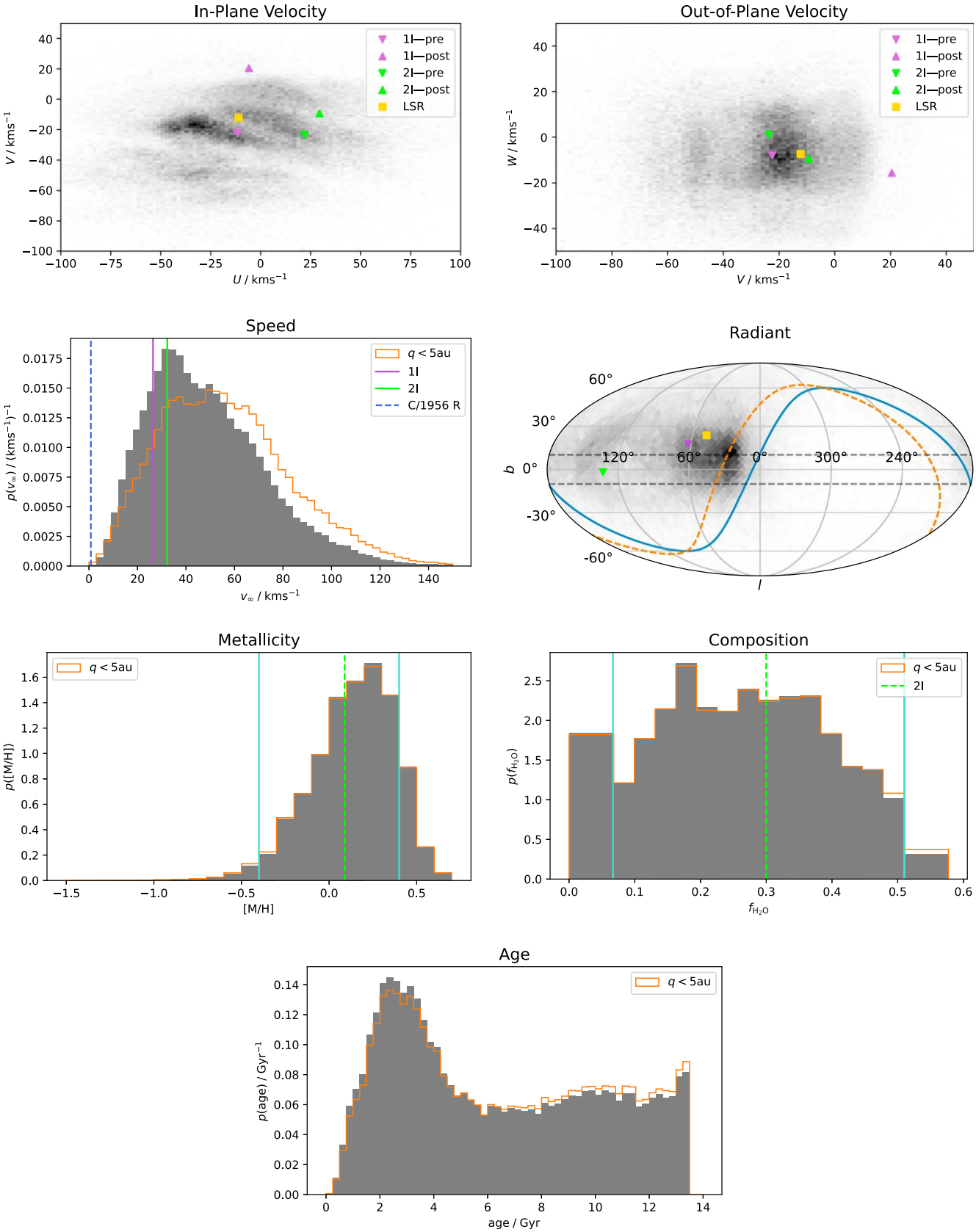

Figure B1. The solar neighborhood ISO distribution, without including the volume sampling rate. The distribution of $q < 5$ au ISOs of Figure 3 is included as an outline for comparison—there is very little difference apart from the speed distribution.

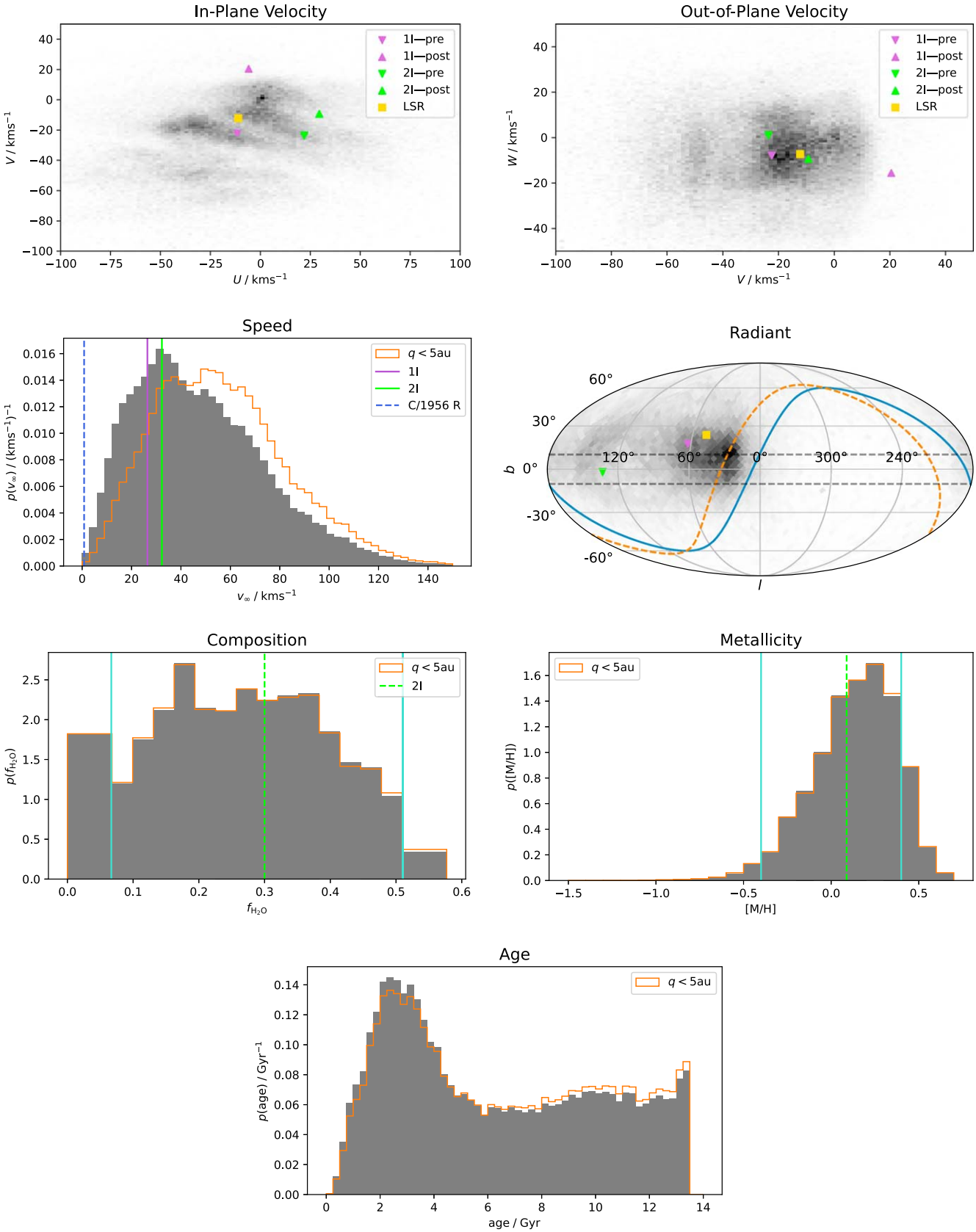

Figure B2. Same as Figure 3 but for ISOs with $q < 1$ au.

applied. In Figure B2, we apply the volume sampling rate for ISOs with perihelia less than 1 au, and in Figure B3 we apply the volume sampling rate for perihelia less than 30 au. For comparison, for each one-dimensional histogram we also plot in an orange line our principal prediction, the ISO distributions for perihelia less than 5 au, as plotted in Figure 3.

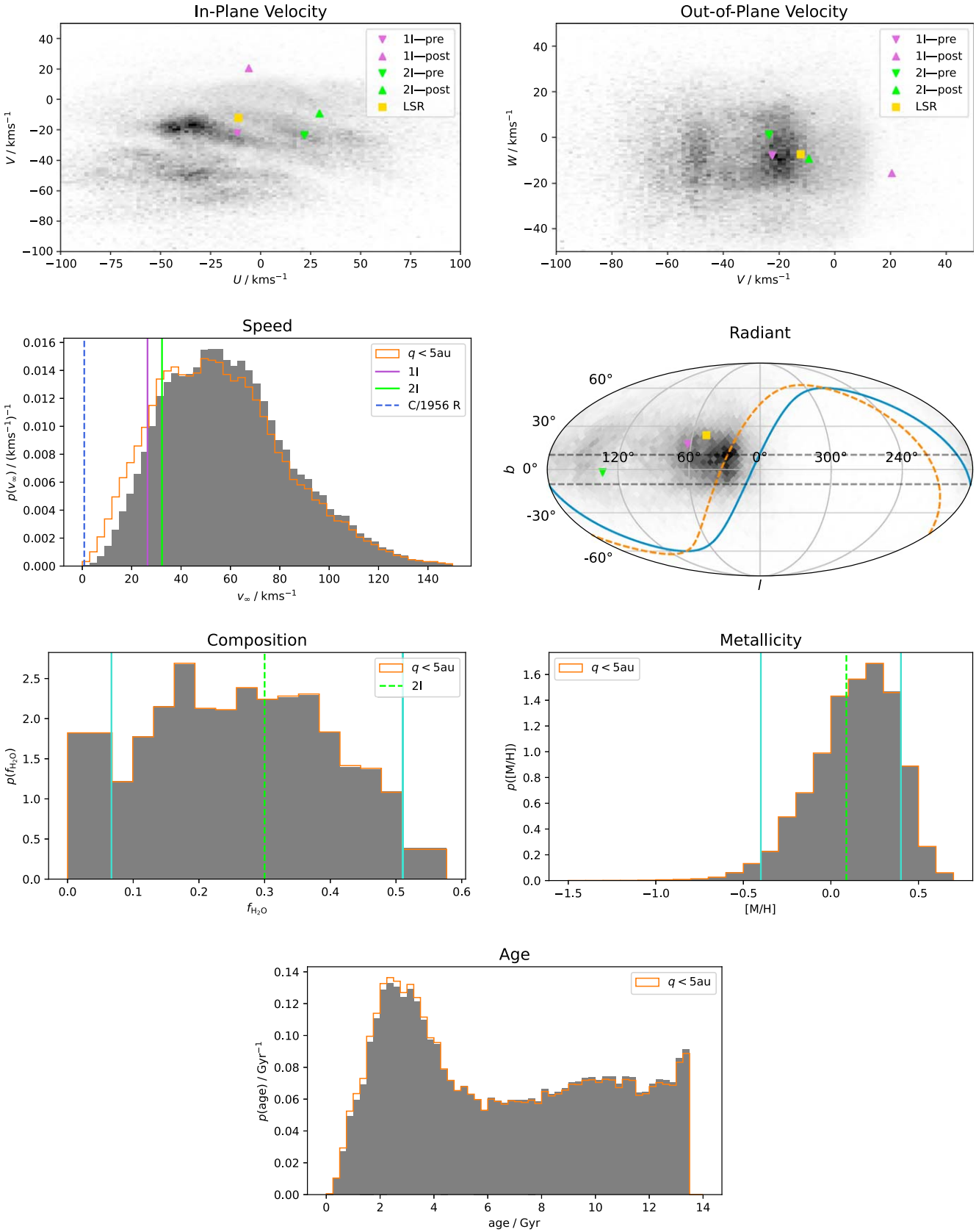

Figure B3. Same as Figure 3 but for ISOs with $q < 30$ au.

Changing the volume sampling rate changes the speed distribution as expected: in Figure B1 the speed distribution is lowered both at high speeds ($v_\infty > 50\,\mathrm{km\,s^{-1}}$) due to the lack of the refresh rate and at very low speeds ($v_\infty < 5\,\mathrm{km\,s^{-1}}$) due to the lack of gravitational focusing; in Figure B2 the speed distribution is shifted toward lower speeds due to the

increased influence of gravitational focusing; and in Figure B3 the speed distribution is shifted toward higher speeds due to the decreased influence of gravitational focusing. There is little difference between any of the age distributions.

Appendix C
Slices Through kNN Density Estimation

This appendix comprises Figure C1, showing slices through the kNN density estimation of the three-dimensional velocity distribution of $q < 5$ au ISOs used in Section 4.2.

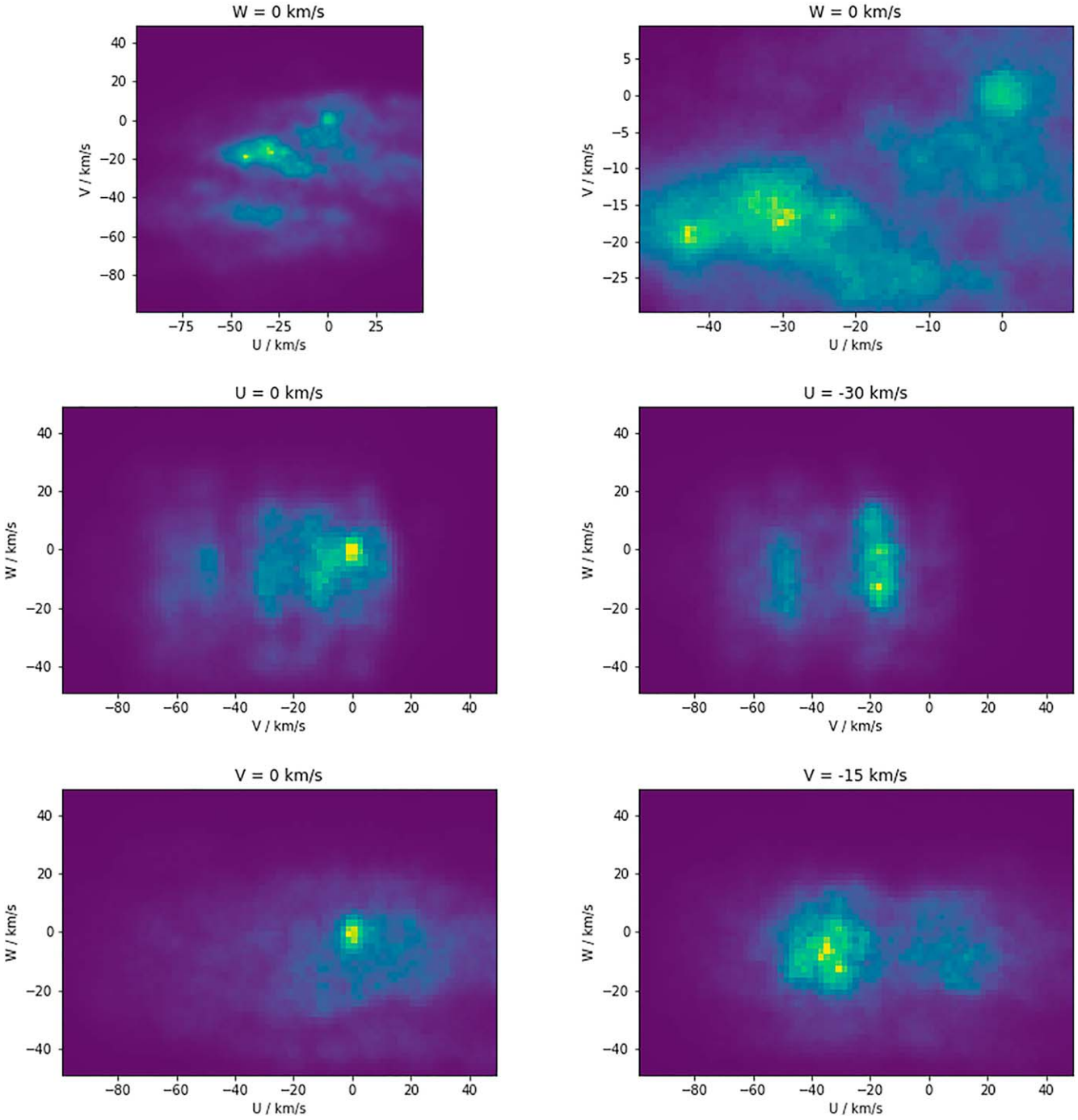

Figure C1. Slices through the continuous three-dimensional velocity distribution of $q < 5$ au ISOs, calculated with the kNN method described in Section 4.2. Slices through the Sun's velocity (U, V, $W = 0, 0, 0$) show a peak caused by gravitational focusing not present in other slices.

ORCID iDs

Matthew J. Hopkins https://orcid.org/0000-0001-6314-873X
Michele T. Bannister https://orcid.org/0000-0003-3257-4490
Chris Lintott https://orcid.org/0000-0001-5578-359X

References

Akaike, H. 1974, ITAC, 19, 716
Almeida-Fernandes, F., & Rocha-Pinto, H. J. 2018, MNRAS, 480, 4903
Anderson, S. E., Rousselot, P., Noyelles, B., Jehin, E., & Mousis, O. 2023, MNRAS, 524, 5182
Antoja, T., Figueras, F., Fernández, D., & Torra, J. 2008, A&A, 490, 135
Antoja, T., Helmi, A., Romero-Gómez, M., et al. 2018, Natur, 561, 360
Baba, J. 2015, MNRAS, 454, 2954
Bailer-Jones, C. A. L., Farnocchia, D., Meech, K. J., et al. 2018, AJ, 156, 205
Bailer-Jones, C. A. L., Farnocchia, D., Ye, Q., Meech, K. J., & Micheli, M. 2020, A&A, 634, A14
Bensby, T., Oey, M. S., Feltzing, S., & Gustafsson, B. 2007, ApJL, 655, L89
Binney, J., & Merrifield, M. 1998, Galactic Astronomy (Princeton, NJ: Princeton Univ. Press)
Binney, J., & Vasiliev, E. 2024, MNRAS, 527, 1915
Bitsch, B., & Battistini, C. 2020, A&A, 633, A10
Bovy, J., Allende Prieto, C., Beers, T. C., et al. 2012, ApJ, 759, 131
Bressan, A., Marigo, P., Girardi, L., et al. 2012, MNRAS, 427, 127
Brown, P. G., & Borovička, J. 2023, ApJ, 953, 167
Burkert, A., & Hensler, G. 1987, in Nuclear Astrophysics, ed. W. Hillebrandt et al., Vol. 287 (Berlin: Springer-Verlag), 159
Cabral, N., Guilbert-Lepoutre, A., Bitsch, B., Lagarde, N., & Diakite, S. 2023, A&A, 673, A117
Cantat-Gaudin, T., Fouesneau, M., Rix, H.-W., et al. 2023, A&A, 669, A55
Castro-Ginard, A., Brown, A. G. A., Kostrzewa-Rutkowska, Z., et al. 2023, A&A, 677, A37
Chabrier, G. 2001, ApJ, 554, 1274
Chabrier, G. 2003, PASP, 115, 763
Chambers, K. C., Magnier, E. A., Metcalfe, N., et al. 2016, arXiv:1612.0556010
Childs, A. C., & Martin, R. G. 2022, ApJL, 935, L31
Cook, N. V., Ragozzine, D., Granvik, M., & Stephens, D. C. 2016, ApJ, 825, 51
Creevey, O. L., & Lebreton, Y. 2022, https://dms.cosmos.esa.int/COSMOS/doc_fetch.php?id=1612899
Creevey, O. L., Sordo, R., Pailler, F., et al. 2023, A&A, 674, A26
Cropper, M., Katz, D., Sartoretti, P., et al. 2018, A&A, 616, A5
Ćuk, M. 2018, ApJL, 852, L15
Daniel, K. J., & Wyse, R. F. G. 2015, MNRAS, 447, 3576
Dehnen, W. 1998, AJ, 115, 2384
Delhaye, J. 1965, in Galactic structure, ed. A. Blaauw & M. Schmidt (Chicago, IL: Univ. Chicago Press), 61
Dybczyński, P. A., & Królikowska, M. 2018, A&A, 610, L11
Dybczyński, P. A., Królikowska, M., & Wysoczańska, R. 2019, arXiv:1909.10952
Eddington, A. S. 1906, MNRAS, 67, 34
Edvardsson, B., Andersen, J., Gustafsson, B., et al. 1993, A&A, 275, 101
Engelhardt, T., Jedicke, R., Vereš, P., et al. 2017, AJ, 153, 133
Eubanks, T. M., Hein, A. M., Lingam, M., et al. 2021, arXiv:2103.03289
Famaey, B., Siebert, A., & Jorissen, A. 2008, A&A, 483, 453
Feng, F., & Jones, H. R. A. 2018, ApJL, 852, L27
Fitzsimmons, A., Meech, K., Matrà, L., & Pfalzner, S. 2023, arXiv:2303.17980
Forbes, J. C., & Loeb, A. 2019, ApJL, 875, L23
Fouesneau, M., Frémat, Y., Andrae, R., et al. 2023, A&A, 674, A28
Francis, P. J. 2005, ApJ, 635, 1348
Gaia Collaboration, Prusti, T., de Bruijne, J., H., J., et al. 2016, A&A, 595, A1
Gaia Collaboration, Smart, R. L., Sarro, L. M., et al. 2021, A&A, 649, A6
Gaia Collaboration, Vallenari, A., Brown, A. G. A., et al. 2023, A&A, 674, A1
Gentile Fusillo, N. P., Tremblay, P. E., Cukanovaite, E., et al. 2021, MNRAS, 508, 3877
Górski, K. M., Hivon, E., Banday, A. J., et al. 2005, ApJ, 622, 759
Green, G. M., Schlafly, E., Zucker, C., Speagle, J. S., & Finkbeiner, D. 2019, ApJ, 887, 93
Guilbert-Lepoutre, A., Besse, S., Mousis, O., et al. 2015, SSRv, 197, 271
Gustafsson, B., Church, R. P., Davies, M. B., & Rickman, H. 2016, A&A, 593, A85
Hands, T. O., Dehnen, W., Gration, A., Stadel, J., & Moore, B. 2019, MNRAS, 490, 21
Haywood, M., Di Matteo, P., Lehnert, M. D., Katz, D., & Gómez, A. 2013, A&A, 560, A109
Heyl, J., Caiazzo, I., & Richer, H. B. 2022, ApJ, 926, 132
Hoover, D. J., Seligman, D. Z., & Payne, M. J. 2022, PSJ, 3, 71
Hopkins, M. J., Lintott, C., Bannister, M. T., Mackereth, J. T., & Forbes, J. C. 2023, AJ, 166, 241
Hunt, J. A. S., Bub, M. W., Bovy, J., et al. 2019, MNRAS, 490, 1026
Hunt, J. A. S., Hong, J., Bovy, J., Kawata, D., & Grand, R. J. J. 2018, MNRAS, 481, 3794
Ivezić, Ž., Kahn, S. M., Tyson, J. A., et al. 2019, ApJ, 873, 111
Jiménez-Esteban, F. M., Torres, S., Rebassa-Mansergas, A., et al. 2023, MNRAS, 518, 5106
Jones, G. H., Snodgrass, C., Tubiana, C., et al. 2024, SSRv, 220, 9
Jönsson, H., Holtzman, J. A., Allende Prieto, C., et al. 2020, AJ, 160, 120
Królikowska, M., & Dones, L. 2023, A&A, 678, A113
Kroupa, P. 2001, MNRAS, 322, 231
Kroupa, P., Weidner, C., Pflamm-Altenburg, J., et al. 2013, in Planets, Stars and Stellar Systems. Volume 5: Galactic Structure and Stellar Populations, ed. T. D. Oswalt & G. Gilmore, Vol. 5 (Berlin: Springer), 115
Lallement, R., Vergely, J. L., Babusiaux, C., & Cox, N. L. J. 2022, A&A, 661, A147
Lian, J., Zasowski, G., Hasselquist, S., et al. 2022, MNRAS, 511, 5639
Lindegren, L., Bastian, U., Biermann, M., et al. 2021, A&A, 649, A4
Lintott, C., Bannister, M. T., & Mackereth, J. T. 2022, ApJL, 924, L1
Lisse, C. M., Gladstone, G. R., Young, L. A., et al. 2022, PSJ, 3, 112
Lu, C. X., Schlaufman, K. C., & Cheng, S. 2020, AJ, 160, 253
Lucchini, S., Pellett, E., D'Onghia, E., & Aguerri, J. A. L. 2023, MNRAS, 519, 432
Marigo, P., Girardi, L., Bressan, A., et al. 2017, ApJ, 835, 77
Marčeta, D. 2023, A&C, 42, 100690
Marčeta, D., & Novaković, B. 2020, MNRAS, 498, 5386
Marčeta, D., & Seligman, D. Z. 2023, PSJ, 4, 230
Mātāmua, R. 2020, in Routledge Handbook of Critical Indigenous Studies, ed. B. Hokowhitu et al., Vol. 4 (1st ed.; Abingdon-on-Thames: Routledge), 230
McGlynn, T. A., & Chapman, R. D. 1989, ApJL, 346, L105
Micheli, M., Farnocchia, D., Meech, K. J., et al. 2018, Natur, 559, 223
Michtchenko, T. A., Lépine, J. R. D., Pérez-Villegas, A., Vieira, R. S. S., & Barros, D. A. 2018, ApJL, 863, L37
Moore, K., Courville, S., Ferguson, S., et al. 2021, P&SS, 197, 105137
Moro-Martìn, A. 2019, ApJL, 872, L32
Moro-Martìn, A., Turner, E. L., & Loeb, A. 2009, ApJ, 704, 733
Nordström, B., Mayor, M., Andersen, J., et al. 2004, A&A, 418, 989
Parenago, P. P. 1951, TrSht, 20, 26
Pfalzner, S., Aizpuru Vargas, L. L., Bhandare, A., & Veras, D. 2021, A&A, 651, A38
Pfalzner, S., & Bannister, M. T. 2019, ApJL, 874, L34
Quillen, A. C., Dougherty, J., Bagley, M. B., Minchev, I., & Comparetta, J. 2011, MNRAS, 417, 762
Rafikov, R. R. 2018, ApJ, 861, 35
Ramos, P., Antoja, T., & Figueras, F. 2018, A&A, 619, A72
Rebassa-Mansergas, A., Maldonado, J., Raddi, R., et al. 2021, MNRAS, 505, 3165
Recio-Blanco, A., de Laverny, P., Kordopatis, G., et al. 2014, A&A, 567, A5
Recio-Blanco, A., de Laverny, P., Palicio, P. A., et al. 2023, A&A, 674, A29
Salaris, M., & Cassisi, S. 2005, Evolution of Stars and Stellar Populations (Weinheim: Wiley-VCH)
Sánchez, J. P., Morante, D., Hermosin, P., et al. 2021, AcAau, 188, 265
Santos, N. C., Adibekyan, V., Mordasini, C., et al. 2015, A&A, 580, L13
Schönrich, R., & Binney, J. 2009, MNRAS, 399, 1145
Schönrich, R., Binney, J., & Dehnen, W. 2010, MNRAS, 403, 1829
Sekanina, Z. 1968, BAICz, 19, 343
Sekanina, Z. 1976, Icarus, 27, 123
Seligman, D., & Laughlin, G. 2018, AJ, 155, 217
Seligman, D. Z., Rogers, L. A., Cabot, S. H. C., et al. 2022, PSJ, 3, 150
Sellwood, J. A., & Binney, J. J. 2002, MNRAS, 336, 785
Skuljan, J., Hearnshaw, J. B., & Cottrell, P. L. 1999, MNRAS, 308, 731
Stern, S. A. 1990, PASP, 102, 793
Trick, W. H., Fragkoudi, F., Hunt, J. A. S., Mackereth, J. T., & White, S. D. M. 2021, MNRAS, 500, 2645
Whipple, F. L. 1975, AJ, 80, 525
Zhao, J., Zhao, G., & Chen, Y. 2009, ApJL, 692, L113
Zhao, P., & Lai, L. 2020, arXiv:2010.00438